ResearchGate

See discussions, stats, and author profiles for this publication at: https://www.researchgate.net/publication/330162407

An implicit mesh discontinuous Galerkin formulation for higher-order plate theories

Article *in* Mechanics of Advanced Materials and Structures · August 2018

DOI: 10.1080/15376494.2018.1516258

CITATIONS
23

READS
360

3 authors:

Vincenzo Gulizzi
Università degli Studi di Palermo
66 PUBLICATIONS **703** CITATIONS
SEE PROFILE

Ivano Benedetti
Università degli Studi di Palermo
142 PUBLICATIONS **1,651** CITATIONS
SEE PROFILE

Alberto Milazzo
Università degli Studi di Palermo
175 PUBLICATIONS **2,092** CITATIONS
SEE PROFILE

All content following this page was uploaded by Vincenzo Gulizzi on 16 January 2019.

The user has requested enhancement of the downloaded file.

An implicit mesh discontinuous Galerkin formulation for higher-order plate theories

V. Gulizzi[a], I. Benedetti[a] and A. Milazzo[a]

[a] Department of Civil, Environmental, Aerospace, and Materials Engineering - DICAM, Università degli Studi di Palermo, Viale delle Scienze, Edificio 8, Palermo, 90128, Italy.

ARTICLE HISTORY

Compiled August 13, 2018

ABSTRACT

In this work, a discontinuous Galerkin formulation for higher-order plate theories is presented. The starting point of the formulation is the strong form of the governing equations, which are derived in the context of the Generalized Unified Formulation and the Equivalent Single Layer approach from the Principle of Virtual Displacements. To express the problem within the discontinuous Galerkin framework, an auxiliary flux variable is introduced and the governing equations are rewritten as a system of first-order partial differential equations, which are weakly stated over each mesh element. The link among neighbouring mesh elements is then retrieved by introducing suitably defined numerical fluxes, whose explicit expressions define the proposed Interior Penalty discontinuous Galerkin formulation. Furthermore, to account for the presence of generally curved boundaries of the considered plate domain, the discretisation mesh is built by combining a background grid and an implicit representation of the domain. *hp*-convergence analyses and a comparison with the results obtained using the Finite Element Method are provided to show the accuracy of the proposed formulation as well as the computational savings in terms of overall degrees of freedom.

KEYWORDS

Interior Penalty discontinuous Galerkin; Generalized Unified Formulation; Equivalent Single Layer plate theories; Implicitly defined mesh; Multilayered plates

1. Introduction

The combination of multiple layers of different materials is a widely employed design strategy in engineering to design advanced structures with enhanced properties. An emblematic example is

provided by multilayered composite plates, which are widely employed for structural applications in aerospace, automotive and naval engineering.

Anisotropy and materials mismatch of multilayered structures induce a non-trivial distributions of stresses, which must be accurately resolved during the design process, particularly in the regions of stress concentration such as holes and cutouts where usually damage onsets and failure occurs. Analytical or closed-form solutions are generally not available and therefore the design of composite multilayered structures is typically supported by numerical tools. Fully three-dimensional (3D) numerical models provide very accurate solutions but they are extremely costly and can become prohibitive in many cases. To overcome this issue, two-dimensional (2D) models have been developed on the basis of suitable assumptions on the behavior of the primary variables throughout the thickness of the considered multilayered structure. They are typically formulated from variational principles and can be subdivided into those stemming from the Principle of Virtual Displacements (PVD) and those stemming from the Reissner Mixed Variational Theorem (RMVT). Again, the 2D plate models can be subdivided into: i) Equivalent Single Layer (ESL) models, which are based on the expansion of the primary variables through *known* functions of the thickness coordinate defined throughout the whole thickness of the considered plate, and ii) Layer-Wise (LW) models where the primary variables are expanded throughout the thickness of the multilayered structures on a per-layer basis and the continuity at the layers' interface is enforced subsequently

Many of the 2D models proposed in the literature are based on the two most common plate theories, namely the Classical Laminated Plate Theory (CLPT) [31] and the First-order Shear Deformation Theory (FSDT) [43, 36], which assume a linear dependence of the in-plane displacements and constant transverse displacement with respect to the thickness coordinate. However, in some cases, especially when high accuracy throughout the plate thickness and local effects are of interest, these models might result limited or even inaccurate. For such a reason, more advanced plate theories, usually referred to as *higher-order* plate theories, have been proposed in the literature by suitably refining the through-the-thickness assumptions on the primary variables in the context of both ESL and LW variable description [6].

A unified treatment of multilayered plate 2D models was proposed by Carrera through the Carrera Unified Formulation (CUF) [8, 9, 7, 10]. The CUF introduces the so-called *fundamental nuclei*, whose expression does not depend on the specific plate theory but on the chosen primary variables of the problem. As a result, ESL and LW fifferent order theories can be written in a compact unified fashion by suitably combining the fundamental nuclei. In the CUF, the primary

variables are expanded throughout the thickness using the same order. A generalization of the CUF was developed by Demasi [16, 17, 18], who proposed to use a different order of expansion for each primary variable by introducing the Generalized Unified Formulation (GUF) Recently, in the framework of the CUF and GUF, D'Ottavio and co-workers [20, 21] proposed to treat groups of layers, the so called sub-laminates, according to the ESL approach and then retrieve the mechanical behavior of the whole assembly by applying the LW approach over the sublaminates. This technique can limit the computational cost of the standard LW approaches and improve the flexibility of the unified formulations of higher-order plate theories.

The standard and largely employed approach for solving the 2D plate theories governing equations is the Finite Element Method (FEM), e.g. [38, 41, 22, 30, 9, 15, 11]) FEM solutions heavily rely upon the quality of the generated mesh; domains of analysis characterized by complex geometries require ad-hoc meshing procedure and typically involve a long pre-processing stage. To reduce the meshing effort, different numerical techniques have been proposed as alternatives to the FEM in the context of plate theories; these include meshless approaches using radial basis functions [24, 25]the Generalized Differential Quadrature [26, 49], the Ritz method [32, 48, 33, 34, 35], and boundary integral formulations [13, 14, 28]. The above numerical techniques are based on a continuous representation of the unknown fields over the domain of analysis and might suffer from limited flexibility when adaptive mesh refinement or non-matching meshes are needed. A powerful numerical technique in this sense is the discontinuous Galerkin (dG) method [2], which, upon admitting a discontinuous approximation of the unknown fields among the mesh elements, can easily handle non-matching and/or hierarchical meshes with hanging nodes, non standard meshes such as polygonal meshes and approximations with different order among the elements. Discontinuous Galerkin methods for the problems of linear and non-linear plate/shell problems have been presented using the CLPT [23, 50, 37, 4] and the FSDT [3, 27, 5, 47] and, to the best of the Authors' knowledge, are not available for general higher-order plate theories.

In this work, an Interior Penalty discontinuous Galerkin formulation for higher-order plate ESL theories within the linear elastic regime is presented. The starting points of the formulation are *i*) a suitable description of the through-the-thickness displacement field introduced according to the GUF and the ESL approach, and *ii*) the strong form of the corresponding set of second-order partial differential equations obtained by means of the PVD. To place the considered problem within the framework of dG methods, an auxiliary flux variable is first introduced and the system of second-order partial differential equations is rewritten as a system of first-

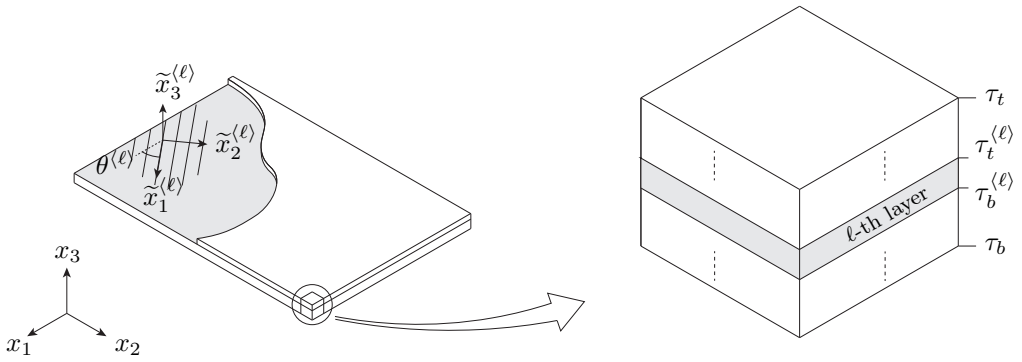

Figure 1.: Schematic representation of a multilayered composite plate.

order partial differential equations, which are stated in weak form over each mesh element. Then, by suitably specifying the expression of the numerical fluxes at the interfaces between contiguous mesh elements and at the boundaries of the considered domain, the proposed Interior Penalty discontinuous formulation is derived. Regarding the meshing strategy, the developed formulation is coupled with the implicitly defined mesh technique developed by Saye [45, 46], which allows to resolve curved boundaries with high-order accuracy by combining an easy-to-generate background grid and the implicit representation of the domain of analysis. The reported results show the effect of the penalty parameter, optimal *hp*-convergence and a satisfactory comparison between the present formulation and standard FEM.

2. Problem statement

A multilayered plate referred to a global reference system $x_1x_2x_3$ as shown in Fig.(1) is considered. The plate occupies the domain V and its boundary is indicated by ∂V; The bottom and top faces lie in the plane $x_3 = \tau_b$ and $x_3 = \tau_t$, respectively, and $\tau \equiv \tau_t - \tau_b$ represents the thickness of the plate. The plate consists of N_ℓ layers and, in the following, a quantity referring to the ℓ-th layer is denoted by the superscript $\langle\ell\rangle$. The ℓ-th layer has the bottom and top faces located at $x_3 = \tau_b^{\langle\ell\rangle}$ and $x_3 = \tau_t^{\langle\ell\rangle}$, respectively, and it has a fibers orientation angle $\theta^{\langle\ell\rangle}$, which defines a layer's local reference system $\widetilde{x}_1^{\langle\ell\rangle}\widetilde{x}_2^{\langle\ell\rangle}\widetilde{x}_3^{\langle\ell\rangle}$ such that the $\widetilde{x}_3^{\langle\ell\rangle}$ direction is aligned with the x_3 direction and the axes $\widetilde{x}_1^{\langle\ell\rangle}$-$\widetilde{x}_2^{\langle\ell\rangle}$ are rotated with respect to the axes x_1-x_2 of the angle $\theta^{\langle\ell\rangle}$.

Using the above notation, the volume V of the whole plate can be identified by the points belonging to the product space $\Omega \times [\tau_b, \tau_t]$ where $\Omega \subset \mathbb{R}^2$ denotes the *modeling domain* for the composite plate and $[\tau_b, \tau_t]$ is the thickness interval. Similarly, the volume $V^{\langle\ell\rangle}$ of the ℓ-th layer

can be identified by the points belonging to $\Omega \times [\tau_b^{\langle \ell \rangle}, \tau_t^{\langle \ell \rangle}]$.

Eventually, the following notation is introduced: $\boldsymbol{u} = \{u_1, u_2, u_3\}^\intercal$ denotes the displacement field, $\boldsymbol{b} = \{b_1, b_2, b_3\}^\intercal$ denotes the body forces acting on the volume of the plate and $\boldsymbol{t} = \{t_1, t_2, t_3\}^\intercal$ denotes the surface tractions acting on the surface of the plate. Moreover, using the Voigt notation, $\boldsymbol{\gamma} = \{\gamma_{11}, \gamma_{22}, \gamma_{33}, \gamma_{32}, \gamma_{31}, \gamma_{12}\}^\intercal$ and $\boldsymbol{\sigma} = \{\sigma_{11}, \sigma_{22}, \sigma_{33}, \sigma_{32}, \sigma_{31}, \sigma_{12}\}^\intercal$ denote the stress and strain fields, respectively.

2.1. *Layer's constitutive behavior*

Each layer of the composite plate is assumed to be homogeneous and linear elastic. In the ℓ-th layer's local reference system $\widetilde{x}_1^{\langle \ell \rangle} \widetilde{x}_2^{\langle \ell \rangle} \widetilde{x}_3^{\langle \ell \rangle}$ the stress-strain relationships is written as

$$\widetilde{\boldsymbol{\sigma}}^{\langle \ell \rangle} = \widetilde{\boldsymbol{c}}^{\langle \ell \rangle} \widetilde{\boldsymbol{\gamma}}^{\langle \ell \rangle} \tag{1}$$

where $\widetilde{\boldsymbol{c}}^{\langle \ell \rangle}$ is a 6×6 matrix containing the stiffness coefficients. In the plate reference system, see Fig.(1), the layer's constitutive law (1) can be written as

$$\boldsymbol{\sigma}^{\langle \ell \rangle} = \boldsymbol{c}^{\langle \ell \rangle} \boldsymbol{\gamma}^{\langle \ell \rangle}, \tag{2}$$

where $\boldsymbol{\sigma}^{\langle \ell \rangle} = \mathbf{T}_\sigma^{-1}(\theta^{\langle \ell \rangle}) \widetilde{\boldsymbol{\sigma}}^{\langle \ell \rangle}$, $\boldsymbol{\gamma}^{\langle \ell \rangle} = \mathbf{T}_\gamma^{-1}(\theta^{\langle \ell \rangle}) \widetilde{\boldsymbol{\gamma}}^{\langle \ell \rangle}$, $\boldsymbol{c}^{\langle \ell \rangle} = \mathbf{T}_\sigma^{-1}(\theta^{\langle \ell \rangle}) \widetilde{\boldsymbol{c}}^{\langle \ell \rangle} \mathbf{T}_\gamma(\theta^{\langle \ell \rangle})$ and $\mathbf{T}_\sigma(\theta)$ and $\mathbf{T}_\gamma(\theta)$ are suitable transformation matrices, whose expression can be found in Ref.[29].

2.2. *Strain-displacements relationship*

Upon adopting the small strains assumption, the strain-displacements relationship are written by separating the derivatives with respect to the coordinates x_1, x_2 and x_3. In particular, given the displacement field $\boldsymbol{u}$ at the generic point within the plate, the strain $\boldsymbol{\gamma}$ can be written as

$$\boldsymbol{\gamma} = \boldsymbol{I}_1 \frac{\partial \boldsymbol{u}}{\partial x_1} + \boldsymbol{I}_2 \frac{\partial \boldsymbol{u}}{\partial x_2} + \boldsymbol{I}_3 \frac{\partial \boldsymbol{u}}{\partial x_3} = \boldsymbol{I}_\lambda \frac{\partial \boldsymbol{u}}{\partial x_\lambda} + \boldsymbol{I}_3 \frac{\partial \boldsymbol{u}}{\partial x_3}, \tag{3}$$

where

$$\boldsymbol{I}_1 \equiv \begin{bmatrix} 1 & 0 & 0 \\ 0 & 0 & 0 \\ 0 & 0 & 0 \\ 0 & 0 & 0 \\ 0 & 0 & 1 \\ 0 & 1 & 0 \end{bmatrix}, \quad \boldsymbol{I}_2 \equiv \begin{bmatrix} 0 & 0 & 0 \\ 0 & 1 & 0 \\ 0 & 0 & 0 \\ 0 & 0 & 1 \\ 0 & 0 & 0 \\ 1 & 0 & 0 \end{bmatrix} \quad \text{and} \quad \boldsymbol{I}_3 \equiv \begin{bmatrix} 0 & 0 & 0 \\ 0 & 0 & 0 \\ 0 & 0 & 1 \\ 0 & 1 & 0 \\ 1 & 0 & 0 \\ 0 & 0 & 0 \end{bmatrix}. \tag{4}$$

In Eq.(3), for the sake of the readability the second equality has been written upon considering the Einstein summation convention over repeated subscripts, which will be used in the following part of the paper for subscripts taking values of 1 and 2 only.

2.3. *Generalized Unified Formulations*

As introduced in Section (1), the main ingredients of the unified formulations for the mechanical behavior of elastic composite plates are: *i*) the selection of the primary variables (typically either displacement components or displacement and transverse stress components) and the corresponding variational statement (Principle of Virtual Displacements or Reissner Mixed Variational Theorem, respectively); *ii*) the expression of the unknown primary variables as the sum of products of known through-the-thickness functions and unknown generalized in-plane displacement functions, where the order of expansion can be the same for all the variables [7] or independently selected for each component [16]; *iii*) the assumptions that such expansions are valid at the level of the whole plate assembly, at the level of each layer or at the level of groups of layers [20, 21].

The formulation presented in this work is based on the expansions of the displacement components only, which are independently treated through the plate thickness, and on the hypothesis that such expansions are valid at the level of the plate assembly. The present formulation then falls within the displacement-based GUF and the ESL approach. Thus, the i-th component of displacement field for the plate is written as

$$u_i^{\langle \ell \rangle}(x_1, x_2, x_3) = \sum_{\alpha=0}^{N_{u_i}} u_{i\alpha}(x_1, x_2) f_\alpha(x_3), \quad \forall \ell = 1, \ldots, N_\ell, \tag{5}$$

where $f_\alpha(x_3)$ denotes the known through-the-thickness functions, $u_{i\alpha}(x_1, x_2)$ denotes the un-

known generalized displacement functions and $N_{u_i}+1$ is the order of expansion introduced for u_i. The theories obtained with such an approximation are denoted by the notation $\mathrm{ED}_{N_{u_1}N_{u_2}N_{u_3}}$[19], where the symbol E denotes the ESL hypothesis, D denotes the use of the PVD and the three subscripts denote the order of expansion of the three displacement components. It is worth noting that the FSDT corresponds to the ED_{110} theory provided that the plate-stress reduced stiffness matrix is used in Eq.(1). Eq.(5) can be rewritten in matricial notation as

$$\boldsymbol{u}^{\langle\ell\rangle} = \boldsymbol{F}(x_3)\boldsymbol{U}(x_1, x_2), \quad \forall \ell = 1, \ldots, N_\ell, \tag{6}$$

where $\boldsymbol{U}$ is a $(N_{u_1} + N_{u_2} + N_{u_3} + 3) \times 1$ vector collecting the generalized displacement functions and, consistently, $\boldsymbol{F}$ is a $3 \times (N_{u_1} + N_{u_2} + N_{u_3} + 3)$ matrix collecting the through-the-thickness functions. To exemplify the definition of the vector $\boldsymbol{U}$ and the matrix $\boldsymbol{F}$, if the FSDT is chosen, $\boldsymbol{U}$ and $\boldsymbol{F}$ would be:

$$\boldsymbol{U} = \{u, v, w, \phi_x, \phi_y\}^\intercal \quad \text{and} \quad \boldsymbol{F} = \begin{bmatrix} 1 & 0 & 0 & x_3 & 0 \\ 0 & 1 & 0 & 0 & x_3 \\ 0 & 0 & 1 & 0 & 0 \end{bmatrix}, \tag{7}$$

where u, v and w denote the displacement components of a point on the plane $x_3 = 0$ and ϕ_x and ϕ_y are the rotations about the y- and x-axes [42].

Upon introducing Eq.(6) into Eq.(3), the strain field is also written in term of an expansion of in-plane and through-the-thickness functions as

$$\boldsymbol{\gamma}^{\langle\ell\rangle} = \boldsymbol{I}_\lambda \boldsymbol{F} \frac{\partial \boldsymbol{U}}{\partial x_\lambda} + \boldsymbol{I}_3 \frac{\mathrm{d}\boldsymbol{F}}{\mathrm{d}x_3}\boldsymbol{U}, \quad \forall \ell = 1, \ldots, N_\ell. \tag{8}$$

Eventually, the stress field is obtained by substituting Eq.(8) into Eq.(2).

2.4. *Governing equations*

The strong form of the governing equations are derived by means of the Principle of Virtual Displacements, which, for the plate assembly, is written as

$$\sum_{\ell=1}^{N_\ell} \int_{V^{\langle\ell\rangle}} \delta\boldsymbol{\gamma}^{\langle\ell\rangle\intercal} \boldsymbol{\sigma}^{\langle\ell\rangle} = \sum_{\ell=1}^{N_\ell} \int_{V^{\langle\ell\rangle}} \delta\boldsymbol{u}^{\langle\ell\rangle\intercal} \boldsymbol{b}^{\langle\ell\rangle} + \sum_{\ell=1}^{N_\ell} \int_{\partial V^{\langle\ell\rangle}} \delta\boldsymbol{u}^{\langle\ell\rangle\intercal} \boldsymbol{t}^{\langle\ell\rangle}. \tag{9}$$

where it is assumed that $\boldsymbol{\gamma}^{\langle\ell\rangle} = \boldsymbol{\gamma}(\boldsymbol{U})$ by means of Eq.(8) and $\boldsymbol{\sigma}^{\langle\ell\rangle} = \boldsymbol{\sigma}^{\langle\ell\rangle}(\boldsymbol{U})$ by means of Eqs.(2) and (8). In Eq.(9) and for the remaining part of this work, the differential indicating the measure of integration is dropped as it is clear by means of the domain of integration. Upon substituting Eqs.(6), (8) and (2) into Eq.(9) and integrating along the thickness, one obtains the following expression of the PVD for the considered plate theories

$$\int_{\Omega} \frac{\partial \delta \boldsymbol{U}^{\intercal}}{\partial x_{\lambda}} \left(\boldsymbol{Q}_{\lambda\mu} \frac{\partial \boldsymbol{U}}{\partial x_{\mu}} + \boldsymbol{R}_{\lambda 3} \boldsymbol{U} \right) + \delta \boldsymbol{U}^{\intercal} \left(\boldsymbol{R}_{\lambda 3}^{\intercal} \frac{\partial \boldsymbol{U}}{\partial x_{\lambda}} + \boldsymbol{S}_{33} \boldsymbol{U} \right) = \int_{\Omega} \delta \boldsymbol{U}^{\intercal} \overline{\boldsymbol{B}} + \int_{\partial\Omega} \delta \boldsymbol{U}^{\intercal} \boldsymbol{T}. \quad (10)$$

In Eq.(10), the matrices $\boldsymbol{Q}_{\lambda\mu}$, $\boldsymbol{R}_{\lambda 3}$, with $\lambda, \mu = 1, 2$, and $\boldsymbol{S}_{33}$ denote the generalized stiffness matrices defined by means of the following integrals over the layers' thickness

$$\boldsymbol{Q}_{\lambda\mu} \equiv \sum_{\ell=1}^{N_{\ell}} \int_{\tau_b^{\langle\ell\rangle}}^{\tau_t^{\langle\ell\rangle}} \boldsymbol{F}^{\intercal} \boldsymbol{I}_{\lambda}^{\intercal} \boldsymbol{c}^{\langle\ell\rangle} \boldsymbol{I}_{\mu} \boldsymbol{F}, \quad (11a)$$

$$\boldsymbol{R}_{\lambda 3} \equiv \sum_{\ell=1}^{N_{\ell}} \int_{\tau_b^{\langle\ell\rangle}}^{\tau_t^{\langle\ell\rangle}} \boldsymbol{F}^{\intercal} \boldsymbol{I}_{\lambda}^{\intercal} \boldsymbol{c}^{\langle\ell\rangle} \boldsymbol{I}_3 \frac{\mathrm{d}\boldsymbol{F}}{\mathrm{d}x_3}, \quad (11b)$$

and

$$\boldsymbol{S}_{33} \equiv \sum_{\ell=1}^{N_{\ell}} \int_{\tau_b^{\langle\ell\rangle}}^{\tau_t^{\langle\ell\rangle}} \frac{\mathrm{d}\boldsymbol{F}^{\intercal}}{\mathrm{d}x_3} \boldsymbol{I}_3^{\intercal} \boldsymbol{c}^{\langle\ell\rangle} \boldsymbol{I}_3 \frac{\mathrm{d}\boldsymbol{F}}{\mathrm{d}x_3}. \quad (11c)$$

Similarly, the vectors $\overline{\boldsymbol{B}}$ and $\boldsymbol{T}$ denote the generalized volume and boundary loads, respectively, defined as

$$\overline{\boldsymbol{B}} \equiv \boldsymbol{F}^{\intercal}(x_3 = \tau_b) \bar{\boldsymbol{t}} + \boldsymbol{F}^{\intercal}(x_3 = \tau_t) \bar{\boldsymbol{t}} + \sum_{\ell=1}^{N_{\ell}} \int_{\tau_b^{\langle\ell\rangle}}^{\tau_t^{\langle\ell\rangle}} \boldsymbol{F}^{\intercal} \boldsymbol{b}^{\langle\ell\rangle} \quad (12a)$$

$$\boldsymbol{T} \equiv \sum_{\ell=1}^{N_{\ell}} \int_{\tau_b^{\langle\ell\rangle}}^{\tau_t^{\langle\ell\rangle}} \boldsymbol{F}^{\intercal} \bar{\boldsymbol{t}}^{\langle\ell\rangle}, \quad (12b)$$

where $\bar{\boldsymbol{t}}$ denotes the prescribed surface tractions over the surfaces of the plate. Eventually, it is recalled that in Eq.(10) Ω is the modeling domain of the plate spanned by the coordinates x_1 and x_2 and $\partial\Omega$ is its boundary.

The strong form of the governing equations are then derived by integrating by parts Eq.(10) and noting that the variational statement must be valid for any virtual generalized displacement vector $\delta \boldsymbol{U}$. In fact, one obtains the following set of second order partial different equations

$$-\frac{\partial}{\partial x_\lambda}\left(\boldsymbol{Q}_{\lambda\mu}\frac{\partial \boldsymbol{U}}{\partial x_\mu}+\boldsymbol{R}_{\lambda 3}\boldsymbol{U}\right)+\boldsymbol{R}^{\intercal}_{\lambda 3}\frac{\partial \boldsymbol{U}}{\partial x_\lambda}+\boldsymbol{S}_{33}\boldsymbol{U}=\overline{\boldsymbol{B}}, \quad \text{in } \Omega, \tag{13}$$

subjected to the following set of boundary conditions

$$\begin{cases} n_\lambda\left(\boldsymbol{Q}_{\lambda\mu}\frac{\partial \boldsymbol{U}}{\partial x_\mu}+\boldsymbol{R}_{\lambda 3}\boldsymbol{U}\right)=\overline{\boldsymbol{T}}, & \text{on } \partial\Omega_N \\ \boldsymbol{U}=\overline{\boldsymbol{U}}, & \text{on } \partial\Omega_D \end{cases}, \tag{14}$$

where n_λ is the λ-th component of the outward unit normal of the modeling domain boundary $\partial\Omega$, $\partial\Omega_D \subset \partial\Omega$ is the part of the boundary where the Dirichlet boundary conditions are prescribed, and $\partial\Omega_N \subset \partial\Omega$ is the part of the boundary where the Neumann boundary conditions are prescribed. The boundary conditions as written in Eq.(14) assume that the boundary $\partial\Omega_D$ or $\partial\Omega_N$ is the same for all the functions contained in $\boldsymbol{U}$. However, in general $\partial\Omega_D$ or $\partial\Omega_N$ can be different for each functions in $\boldsymbol{U}$ but this aspect does not represent a restriction for the formulation as it will be shown in the numerical tests.

As discussed in Section (1), the through-the-thickness expansions introduced with plate higher-order theories allows to transform the equations of three-dimensional elasticity to two-dimensional partial differential equations as given in Eq.(13), which are solved over the 2D modeling domain Ω and are subjected to the boundary conditions (14).

3. Discontinuous Galerkin framework

For the solution of the plate governing equations derived in the previous section, a discontinuous Galerkin method is proposed and discussed. Within the dG framework, a flux variable is introduced to transform the governing equations into a first-order system of partial differential equations [2]. In this case, it is convenient to introduce the flux variable

$$\boldsymbol{\Sigma}_\lambda \equiv \boldsymbol{Q}_{\lambda\mu}\frac{\partial \boldsymbol{U}}{\partial x_\mu}+\boldsymbol{R}_{\lambda 3}\boldsymbol{U}, \quad \lambda,\mu=1,2, \tag{15}$$

in such a way that the set of governing equations (13) are equivalently written as

$$-\frac{\partial \boldsymbol{\Sigma}_\lambda}{\partial x_\lambda} + \boldsymbol{R}_{\lambda 3}^\intercal \frac{\partial \boldsymbol{U}}{\partial x_\lambda} + \boldsymbol{S}_{33}\boldsymbol{U} = \overline{\boldsymbol{B}}, \tag{16a}$$

$$\boldsymbol{\Sigma}_\lambda = \boldsymbol{Q}_{\lambda\mu}\frac{\partial \boldsymbol{U}}{\partial x_\mu} + \boldsymbol{R}_{\lambda 3}\boldsymbol{U}. \tag{16b}$$

Let us now suppose that the domain Ω is divided into N_e non-overlapping mesh elements. In the following, quantities referred to the generic e-th mesh element are denoted using the superscript (e). Let us also introduce the space $\mathcal{V}_{hp}$ of discontinuous polynomials defined as

$$\mathcal{V}_{hp} \equiv \{v : \Omega \to \mathbb{R} \mid v|_{\Omega^{(e)}} \in \mathcal{P}_p^{(e)} \ \forall e = 1, \dots, N_e\}$$

where $\mathcal{P}_p^{(e)}$ is the space of the polynomials functions of degree $p \geq 1$ on $\Omega^{(e)}$. Accordingly, the space $\mathcal{V}_{hp}^d$ of discontinuous polynomial vector fields is defined as $\mathcal{V}_{hp}^d \equiv (\mathcal{V}_{hp})^d$. The weak statements of Eqs.(16a) and (16b) over each mesh element $\Omega^{(e)}$ are then derived by introducing the test functions $\boldsymbol{V}, \boldsymbol{\Gamma}_1, \boldsymbol{\Gamma}_2 \in \mathcal{V}_{hp}^{N_u}$, where $N_u = N_{u_1} + N_{u_2} + N_{u_3} + 3$, see Sec.(2.3). More specifically, upon multiplying Eq.(16a) by $\boldsymbol{V}^\intercal$, integrating over the generic element $\Omega^{(e)}$ and using integration by parts, one obtains the weak form of Eq.(16a) as follows

$$\int_{\Omega^{(e)}} \frac{\partial \boldsymbol{V}^\intercal}{\partial x_\lambda}\boldsymbol{\Sigma}_{h\lambda} + \boldsymbol{V}^\intercal\left(\boldsymbol{R}_{\lambda 3}^\intercal\frac{\partial \boldsymbol{U}_h}{\partial x_\lambda} + \boldsymbol{S}_{33}\boldsymbol{U}_h\right) = \int_{\partial\Omega^{(e)}} \boldsymbol{V}^\intercal\widehat{\boldsymbol{\Sigma}}_\lambda n_\lambda + \int_{\Omega^{(e)}} \boldsymbol{V}^\intercal\overline{\boldsymbol{B}}, \tag{17a}$$

where $\partial\Omega^{(e)}$ represents the boundary of $\Omega^{(e)}$. Analogously, the weak form of Eq.(16b) is written as

$$\int_{\Omega^{(e)}} \boldsymbol{\Gamma}_\lambda^\intercal\boldsymbol{\Sigma}_{h\lambda} = \int_{\Omega^{(e)}} \boldsymbol{\Gamma}_\lambda^\intercal\left(\boldsymbol{Q}_{\lambda\mu}\frac{\partial \boldsymbol{U}_h}{\partial x_\mu} + \boldsymbol{R}_{\lambda 3}\boldsymbol{U}_h\right) + \int_{\partial\Omega^{(e)}} (\boldsymbol{\Gamma}_\lambda^\intercal\boldsymbol{Q}_{\lambda\mu} + \boldsymbol{V}^\intercal\boldsymbol{R}_{\mu 3}^\intercal)(\widehat{\boldsymbol{U}} - \boldsymbol{U}_h)n_\mu. \tag{17b}$$

A few comments follow: *i*) $\widehat{\boldsymbol{\Sigma}}_\lambda$ and $\widehat{\boldsymbol{U}}$ appearing in Eqs.(17a) and (17b), respectively, denote the *numerical fluxes*, which are approximations of $\boldsymbol{\Sigma}_\lambda$ and $\boldsymbol{U}$, respectively, on the boundary $\partial\Omega^{(e)}$. The expressions of the numerical fluxes typically specify the adopted dG method and are well known to affect its stability and accuracy as well as the sparsity pattern of the resulting stiffness matrix [12, 2, 40]; *ii*) $\boldsymbol{U}_h$ and $\boldsymbol{\Sigma}_{h\lambda}$ denote the solutions of the weak statement of the governing equations, i.e. Eqs.(17a) and (17b), and are in general approximations of the exact

solutions $\boldsymbol{U}$ and $\boldsymbol{\Sigma}_\lambda$ of Eqs.(16a) and (16b); *iii*) as it will be shown in what follows, the specific form of Eq.(17b) has been chosen to obtain a dG formulation which is symmetric and verifies the *consistency* condition.

To derive the dG formulation of the whole plate domain Ω, some preliminaries are needed. Let us first define $\partial\Omega_D^{(e)} \subset \partial\Omega^{(e)}$ and $\partial\Omega_N^{(e)} \subset \partial\Omega^{(e)}$ as the boundaries of the e-th element where Dirichlet and Neumann boundary conditions are enforced, respectively. It follows that $\partial\Omega_D = \bigcup_{e=1}^{N_e} \partial\Omega_D^{(e)}$ and $\partial\Omega_N = \bigcup_{e=1}^{N_e} \partial\Omega_N^{(e)}$. Recalling that $\Omega = \bigcup_{e=1}^{N_e} \Omega^{(e)}$, the following integral operators are introduced

$$\int_{\Omega_h} \bullet \equiv \sum_{e=1}^{N_e} \int_{\Omega^{(e)}} \bullet^{(e)}, \quad \int_{\partial\Omega_{hD}} \bullet \equiv \sum_{e=1}^{N_e} \int_{\partial\Omega_D^{(e)}} \bullet^{(e)} \quad \text{and} \quad \int_{\partial\Omega_{hN}} \bullet \equiv \sum_{e=1}^{N_e} \int_{\partial\Omega_N^{(e)}} \bullet^{(e)}, \tag{18}$$

where $\bullet^{(e)}$ denotes the integrand functions defined over the corresponding domain of integration. Similarly, let us define $\partial\Omega_I^{(e)} \subset \partial\Omega^{(e)}$ as the boundary that the e-th element shares with neighboring elements, and $\partial\Omega_I$ as the union of all the elements' internal boundaries, i.e. $\partial\Omega_I \equiv \bigcup_e \partial\Omega_I^{(e)}$. It is worth to underline that $\partial\Omega_I$ also coincides with the union of all the *internal* edges of the mesh, that is $\partial\Omega_I = \bigcup_{i=1}^{N_i} I^{(i)}$, where N_i is the total number of mesh edges and $I^{(i)}$ is the i-th edge shared by two generic neighboring elements $\Omega^{(e)}$ and $\Omega^{(e')}$, that is $I^{(i)} = \Omega^{(e)} \cap \Omega^{(e')}$. Consistently with Eq.(18), the following integral operator over the mesh internal edges is introduced

$$\int_{\partial\Omega_{hI}} \bullet \equiv \sum_{i=1}^{N_i} \int_{I^{(i)}} \bullet^{(i)}, \tag{19}$$

where $\bullet^{(i)}$ denotes the integrand functions defined over the edge $I^{(i)}$. Furthermore, it is useful to define the following *average* and *jump* operators

$$\{\bullet\}^{(i)} = \frac{1}{2}\left(\bullet^{(e)} + \bullet^{(e')}\right) \quad \text{and} \quad [\![\bullet]\!]_\lambda^{(i)} = n_\lambda^{(e)} \bullet^{(e)} + n_\lambda^{(e')} \bullet^{(e')}, \tag{20}$$

which are defined for each couple of neighboring elements $\Omega^{(e)}$ and $\Omega^{(e')}$ sharing the interface $I^{(i)}$. Using Eqs.(18) to (20) and noting that $n_\lambda^{(e)} = -n_\lambda^{(e')}$, it is demonstrated that the following identity holds

$$\sum_{e=1}^{N_e} \int_{\partial\Omega^{(e)}} \boldsymbol{V}^\intercal \boldsymbol{\Sigma}_\lambda n_\lambda = \int_{\partial\Omega_{hI}} \{\boldsymbol{V}\}^\intercal [\![\boldsymbol{\Sigma}_\lambda]\!]_\lambda + [\![\boldsymbol{V}]\!]_\lambda^\intercal \{\boldsymbol{\Sigma}_\lambda\} + \int_{\partial\Omega_{hD} \cup \partial\Omega_{hN}} \boldsymbol{V}^\intercal \boldsymbol{\Sigma}_\lambda n_\lambda. \tag{21}$$

This identity is useful to rewrite the element boundary integral appearing in the right-hand sides of Eqs.(17a) and (17b) when the sum over all the mesh elements is considered. Indeed, summing over all the mesh elements and employing the operators defined in Eqs.(18) to (20) as well as the identity given in (21), Eqs.(17a) and (17b) lead to following weak dG statements for the whole plate domain:

$$\int_{\Omega_h} \frac{\partial \boldsymbol{V}^\intercal}{\partial x_\lambda} \boldsymbol{\Sigma}_{h\lambda} + \boldsymbol{V}^\intercal \left(\boldsymbol{R}_{\lambda 3}^\intercal \frac{\partial \boldsymbol{U}_h}{\partial x_\lambda} + \boldsymbol{S}_{33} \boldsymbol{U}_h \right) = \int_{\partial\Omega_{hI}} \{\boldsymbol{V}\}^\intercal [\![\widehat{\boldsymbol{\Sigma}}_\lambda]\!]_\lambda + [\![\boldsymbol{V}]\!]_\lambda^\intercal \{\widehat{\boldsymbol{\Sigma}}_\lambda\} + \\ + \int_{\partial\Omega_{hD} \cup \partial\Omega_{hN}} \boldsymbol{V}^\intercal \widehat{\boldsymbol{\Sigma}}_\lambda n_\lambda + \int_{\Omega_h} \boldsymbol{V}^\intercal \overline{\boldsymbol{B}} \quad (22a)$$

and

$$\int_{\Omega_h} \boldsymbol{\Gamma}_\lambda^\intercal \boldsymbol{\Sigma}_{h\lambda} = \int_{\Omega_h} \boldsymbol{\Gamma}_\lambda^\intercal \left(\boldsymbol{Q}_{\lambda\mu} \frac{\partial \boldsymbol{U}_h}{\partial x_\mu} + \boldsymbol{R}_{\lambda 3} \boldsymbol{U}_h \right) + \\ + \int_{\partial\Omega_{hI}} \{\boldsymbol{\Gamma}_\lambda^\intercal \boldsymbol{Q}_{\lambda\mu} + \boldsymbol{V}^\intercal \boldsymbol{R}_{\mu 3}^\intercal\} [\![\widehat{\boldsymbol{U}} - \boldsymbol{U}_h]\!]_\mu + [\![\boldsymbol{\Gamma}_\lambda^\intercal \boldsymbol{Q}_{\lambda\mu} + \boldsymbol{V}^\intercal \boldsymbol{R}_{\mu 3}^\intercal]\!]_\mu \{\widehat{\boldsymbol{U}} - \boldsymbol{U}_h\} + \\ + \int_{\partial\Omega_{hD} \cup \partial\Omega_{hN}} (\boldsymbol{\Gamma}_\lambda^\intercal \boldsymbol{Q}_{\lambda\mu} + \boldsymbol{V}^\intercal \boldsymbol{R}_{\mu 3}^\intercal)(\widehat{\boldsymbol{U}} - \boldsymbol{U}_h) n_\mu, \quad (22b)$$

respectively. By suitably specializing the numerical fluxes appearing in Eqs.(22a) and (22b), it is possible to obtain different dG formulations. For the scope of this work, an Interior Penalty dG formulation is selected.

3.1. *Interior Penalty formulation*

In the Interior Penalty dG formulation proposed in this work, the numerical fluxes $\widehat{\boldsymbol{U}}$ and $\widehat{\boldsymbol{\Sigma}}_\lambda$ are specialized as follows

$$\widehat{\boldsymbol{U}} = \begin{cases} \{\boldsymbol{U}_h\}, & \text{on } \partial\Omega_{hI} \\ \overline{\boldsymbol{U}}, & \text{on } \partial\Omega_{hD} \\ \boldsymbol{U}_h, & \text{on } \partial\Omega_{hN} \end{cases} \quad (23)$$

and

$$\begin{cases} \widehat{\boldsymbol{\Sigma}}_\lambda = \{\boldsymbol{Q}_{\lambda\mu} \frac{\partial \boldsymbol{U}_h}{\partial x_\mu} + \boldsymbol{R}_{\lambda 3} \boldsymbol{U}_h\} - \mu [\![\boldsymbol{U}_h]\!]_\lambda, & \text{on } \partial\Omega_{hI} \\ \widehat{\boldsymbol{\Sigma}}_\lambda = \boldsymbol{Q}_{\lambda\mu} \frac{\partial \boldsymbol{U}_h}{\partial x_\mu} + \boldsymbol{R}_{\lambda 3} \boldsymbol{U}_h - \mu (\boldsymbol{U}_h - \overline{\boldsymbol{U}}) n_\lambda, & \text{on } \partial\Omega_{hD} \\ n_\lambda \widehat{\boldsymbol{\Sigma}}_\lambda = \overline{\boldsymbol{T}}, & \text{on } \partial\Omega_{hN} \end{cases}, \quad (24)$$

where μ denotes the penalty parameter.

Eventually, setting $\boldsymbol{\Gamma}_\lambda \equiv \partial \boldsymbol{V}/\partial x_\lambda$, and using the numerical fluxes given in Eqs.(23) and (24), Eqs.(22a) and (22b) are combined together to obtain the *primal form* of the proposed Interior Penalty formulation as follows

$$B_{\mathtt{IP}}(\boldsymbol{V}, \boldsymbol{U}_h) = R_{\mathtt{IP}}(\boldsymbol{V}, \overline{\boldsymbol{B}}, \overline{\boldsymbol{T}}, \overline{\boldsymbol{U}}), \tag{25}$$

where

$$\begin{aligned} B_{\mathtt{IP}}(\boldsymbol{V}, \boldsymbol{U}_h) = &\int_{\Omega_h} \frac{\partial \boldsymbol{V}^\intercal}{\partial x_\lambda} \left(\boldsymbol{Q}_{\lambda\mu} \frac{\partial \boldsymbol{U}_h}{\partial x_\mu} + \boldsymbol{R}_{\lambda 3} \boldsymbol{U}_h \right) + \boldsymbol{V}^\intercal \left(\boldsymbol{R}_{\lambda 3}^\intercal \frac{\partial \boldsymbol{U}_h}{\partial x_\lambda} + \boldsymbol{S}_{33} \boldsymbol{U}_h \right) + \\ &- \int_{\partial\Omega_{hI}} [\![\boldsymbol{V}]\!]_\lambda^\intercal \left\{ \boldsymbol{Q}_{\lambda\mu} \frac{\partial \boldsymbol{U}_h}{\partial x_\mu} + \boldsymbol{R}_{\lambda 3} \boldsymbol{U}_h \right\} + \left\{ \frac{\partial \boldsymbol{V}^\intercal}{\partial x_\lambda} \boldsymbol{Q}_{\lambda\mu} + \boldsymbol{V}^\intercal \boldsymbol{R}_{\mu 3}^\intercal \right\} [\![\boldsymbol{U}_h]\!]_\mu + \\ &- \int_{\partial\Omega_{hD}} n_\lambda \boldsymbol{V}^\intercal \left(\boldsymbol{Q}_{\lambda\mu} \frac{\partial \boldsymbol{U}_h}{\partial x_\mu} + \boldsymbol{R}_{\lambda 3} \boldsymbol{U}_h \right) + \left(\frac{\partial \boldsymbol{V}^\intercal}{\partial x_\lambda} \boldsymbol{Q}_{\lambda\mu} + \boldsymbol{V}^\intercal \boldsymbol{R}_{\mu 3}^\intercal \right) \boldsymbol{U}_h n_\mu + \\ &+ \int_{\partial\Omega_{hI}} \mu [\![\boldsymbol{V}]\!]_\lambda^\intercal [\![\boldsymbol{U}_h]\!]_\lambda + \int_{\partial\Omega_{hD}} \mu \boldsymbol{V}^\intercal \boldsymbol{U}_h \end{aligned} \tag{26}$$

and

$$\begin{aligned} R_{\mathtt{IP}}(\boldsymbol{V}, \overline{\boldsymbol{B}}, \overline{\boldsymbol{T}}, \overline{\boldsymbol{U}}) = &\int_{\Omega_h} \boldsymbol{V}^\intercal \overline{\boldsymbol{B}} + \int_{\partial\Omega_{hN}} \boldsymbol{V}^\intercal \overline{\boldsymbol{T}} + \\ &- \int_{\partial\Omega_{hD}} \left(\frac{\partial \boldsymbol{V}^\intercal}{\partial x_\lambda} \boldsymbol{Q}_{\lambda\mu} + \boldsymbol{V}^\intercal \boldsymbol{R}_{\mu 3}^\intercal \right) \overline{\boldsymbol{U}} n_\mu + \int_{\partial\Omega_{hD}} \mu \boldsymbol{V}^\intercal \overline{\boldsymbol{U}}. \end{aligned} \tag{27}$$

It is worth noting that the bilinear form $B_{\mathtt{IP}}(\bullet, \bullet)$ is symmetric and verifies the consistency condition, which ensures that the Galerkin orthogonality holds, i.e.

$$B_{\mathtt{IP}}(\boldsymbol{V}, \boldsymbol{U} - \boldsymbol{U}_h) = 0, \quad \forall \boldsymbol{V} \in \mathcal{V}_{hp}^{N_u},$$

where $\boldsymbol{U}$ is the exact solution of Eqs.(13) and (14).

As the last remark on the discontinuous Galerkin approach to plate higher-order theories, it is interesting to note that, from the present Interior Penalty formulation, it is possible to obtain a pure Penalty formulation by neglecting the second and third integrals from the right-hand side of Eq.(26) and the third integral from the right-hand side of Eq.(27). A comparison between the Interior Penalty and the Penalty dG formulation of plate higher-order theories is reported in Sec.(5).

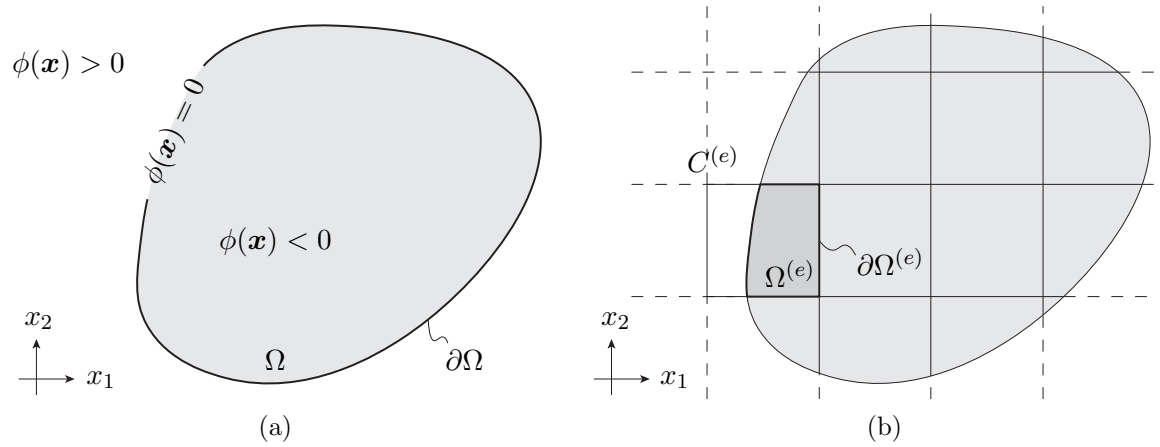

Figure 2.: (a) Implicit representation of the domain Ω through the signed distance function $\phi(\boldsymbol{x})$; (b) Implicit definition of the generic mesh element $\Omega^{(e)}$ and its boundary $\partial\Omega^{(e)}$ as the intersection between the cell $C^{(e)}$ and the domain Ω.

4. Implicitly defined mesh

The formulation presented in the previous section can be employed in conjunction with different domain partion strategies. As an example, it could be easily implemented for generally polygonal meshes and would require only the knowledge of the inter-element neighboring information and a suitable integration procedure for polygonal elements. However, in this work, instead of constructing a mesh whose edges might approximate the boundaries of the considered domain, the implicitly-defined mesh technique for dG methods proposed by Saye [44, 45, 46] is employed. Such a technique offers the advantage of resolving curved boundaries with high-order accuracy, a feature that is highly desirable in weak formulations. The main steps to construct the mesh using Saye's technique are briefly recalled next.

Let us consider a domain Ω and its implicit representation by a suitably defined signed distance function $\phi(\boldsymbol{x})$ such that

$$\Omega = \{\boldsymbol{x} \in \mathbb{R}^2 \mid \phi(\boldsymbol{x}) < 0\} \quad \text{and} \quad \partial\Omega = \{\boldsymbol{x} \in \mathbb{R}^2 \mid \phi(\boldsymbol{x}) = 0\}; \tag{28}$$

let us also consider a background grid covering the whole domain Ω and consisting of a collection of *cells* with typical dimension equal to h. Then, the generic mesh element $\Omega^{(e)}$ is defined as the intersection between the generic cell $C^{(e)}$ of the background grid and the domain Ω, that is:

$$\Omega^{(e)} = C^{(e)} \cap \Omega \quad \text{and} \quad \partial\Omega^{(e)} = (C^{(e)} \cap \partial\Omega) \cup (\partial C^{(e)} \cap \Omega), \tag{29}$$

where $\partial C^{(e)}$ denotes the boundary of the cell $C^{(e)}$. Such a meshing procedure is sketched in

Fig.(2): Fig.(2a) shows the implicit representation of the domain Ω (in grey) and its boundary $\partial\Omega$, whereas Fig.(2b) shows the definition of the generic element $\Omega^{(e)}$ (in darker grey) as the intersection of the cell $C^{(e)}$ and the domain Ω itself.

On the basis of their position with respect to the domain Ω, the background cells are consequently classified into those that fall entirely within Ω, referred to as the *entire* cells [45], those that fall outside Ω, the so-called *empty* cells, and those that are partially within Ω, referred to as the *partial* cells. It is clear that the empty cells do not contribute to the final collection of the mesh elements, whereas the entire cells represent those mesh elements for which the volume and boundary integrals appearing in Eqs.(26) and (27) are computed using standard quadrature schemes; on the other hand, the volume and boundary integrals over the partial cells are evaluated using the quadrature algorithms for implicitly defined volumes and surfaces over n-dimensional hyperrectangles developed by Saye [44]. In such a way, the mesh elements stemming from the partial cells are never explicitly constructed but they are implicitly defined by the distance function $\phi(\boldsymbol{x})$ and the parent background cell. This ensures a high-order resolution of the domain boundaries as well as a high-order accuracy in the enforcement of the boundary conditions. As the last remark on the implicitly-defined mesh, it is noted that it may happen the case when some partial cells have an overly small volume, which would ill-condition the final system. To overcome this issue, small partial cells are merged with neighboring cells leading to the definition of extended mesh elements [45]. Also in this case, extended elements are not explicitly constructed but are defined in terms of neighboring information only. An example of extended elements will be given in the numerical tests of Section (5).

The interested reader is referred to the works of Saye [44, 45, 46] for a more comprehensive description of the implicitly defined mesh and the related quadrature algorithms.

5. Numerical results

In this section, the performances of the developed implicit mesh Interior Penalty discontinuous Galerkin formulation are assessed by considering the elastostatic response of two plate structures, namely a square plate and a square plate with a circular cutout. The two considered plates are shown in Fig.(3): they have sides of length L and a total thickness $\tau = L/10$, while the circular cutout in the plate of Figs.(3b) has radius $r = L/5$.

The plates are subjected to *simply supported* boundary conditions over their four straight

edges, which are enforced by setting $\overline{\boldsymbol{T}} = \mathbf{0}$ in Eq.(27) and by prescribing

$$u_{2\alpha} = u_{3\alpha} = 0, \quad \text{at } x_1 = 0, L, \quad \text{and} \quad u_{1\alpha} = u_{3\alpha} = 0, \quad \text{at } x_2 = 0, L, \tag{30}$$

where the subscript α of the generalized displacement $u_{i\alpha}$ runs from 0 to N_{u_i}. The plates are also subjected to a prescribed surface tractions $\bar{\boldsymbol{t}}$ over their top surface given by

$$\bar{\boldsymbol{t}} = q \sin\left(\frac{\pi x_1}{L}\right) \sin\left(\frac{\pi x_2}{L}\right) \hat{\mathbf{e}}_3, \quad \text{at } x_3 = \tau/2, \tag{31}$$

where q denotes the amplitude and $\hat{\mathbf{e}}_3$ is the unit vector along the x_3-axis; it is worth recalling that he prescribed load given in Eq.(31) contributes to the generalized volume load $\overline{\boldsymbol{B}}$ through the second term of Eq.(12a). The bottom surfaces and the internal lateral surfaces of the cutout shown in Fig.(3b) are traction-free.

The numerical tests are presented using two different materials and three different layups, whose properties are reported in Tables (1) and (2), respectively. In Table (1), E_r denotes a reference stiffness. The three considered plates, namely a single-layer isotropic plate, a single-layer orthotropic plate and a multilayered antisymmetric cross-ply laminate, will be referred to as P_1, P_2 and P_3, respectively, as in Table (2).

Geometry, materials, loads and boundary conditions have been selected since, in the case of the square plate, closed form solution for the 3D case [39] as well as for classical and higher-order plate theories [42, 7, 16] are available in the literature. Eventually, the results are reported in terms of the following non-dimensional quantities

$$\bar{u}_1 = u_1 \left(\frac{\tau^2 E_r}{L^3 q}\right), \quad \bar{u}_3 = u_3 \left(\frac{\tau^3 E_r}{L^4 q}\right),$$

and

$$\bar{\sigma}_{11} = \sigma_{11} \left(\frac{\tau^2}{L^2 q}\right), \quad \bar{\sigma}_{22} = \sigma_{22} \left(\frac{\tau^2}{L^2 q}\right), \quad \bar{\sigma}_{12} = \sigma_{12} \left(\frac{\tau^2}{L^2 q}\right).$$

5.1. *Square plate*

The first set of tests are performed on the square plate shown in Fig.(3a). A cartesian $n \times n$ mesh grid is employed with mesh size equal to $h = L/n$, where n denotes the number of elements

Table 1.: Properties of the considered materials.

Material ID	Property	Component	Value
M_1 (Isotropic)	Young's modulus	E/E_r	1.0
	Poisson's ratio	ν	0.25
M_2 (Orthotropic)	Young's moduli	E_1/E_r	25.0
		E_2/E_r, E_3/E_r	1.0
	Poisson's ratios	ν_{23}, ν_{13}, ν_{12}	0.25
	Shear moduli	G_{23}/E_r	0.2
		G_{13}/E_r, G_{12}/E_r	0.5

Table 2.: Properties of the considered plate sections. The properties of materials M_1 and M_2 are those reported in Tab.(1).

Plate ID	Material	Layup	Layer(s) thickness
P_1 (Single-layer)	M_1	$[0]$	0.1
P_2 (Single-layer)	M_2	$[0]$	0.1
P_3 (Multilayered)	M_2	$[0, 90]_4$	0.0125

along one edge of the plate. To test the accuracy and convergence rate of the proposed dG method, the following ∞-norm error is introduced

$$e(\boldsymbol{U}_h) \equiv \frac{||\boldsymbol{U}_h - \boldsymbol{U}_{\text{exact}}||_\infty}{||\boldsymbol{U}_{\text{exact}}||_\infty}, \tag{32}$$

where $\boldsymbol{U}_h$ denotes the solution computed with dG and $\boldsymbol{U}_{\text{exact}}$ denotes the exact solution.

Figure (4) reports the effect of the penalty parameter μ introduced in Eq.(24) on the error $e(\boldsymbol{U}_h)$ as a function of the polynomial order p a for a 2×2 mesh grid. The results are presented for two different plate theories, namely the FSDT and the ED_{444} theory, and for the three plate layups reported in Tab.(2). The plots show that, after a certain threshold, the error $e(\boldsymbol{U}_h)$ is insensitive to the value of μ, a feature that is highly desirable in dG formulations. Also, it is interesting to note the comparison between the results obtained with the present Interior Penalty dG formulation and those obtained with a pure Penalty formulation, which are reported in Fig.(4a) with solid and dashed lines, respectively. In particular, by fixing the order of the polynomials and the mesh size, it is observed that a much higher value of the penalty parameter is required to achieve the same level of error. This feature is a drawback of pure Penalty methods as significantly increases the condition number of the resolving matrix [2].

Figure (5) report the *hp*-convergence of the ∞-norm error $e(\boldsymbol{U}_h)$ for the present formulation and shows that optimal accuracy is achieved by choosing the penalty parameter μ of order $\mathcal{O}(h^{-1})$ as is typical in the case of Interior Penalty methods for elliptic problems [2].

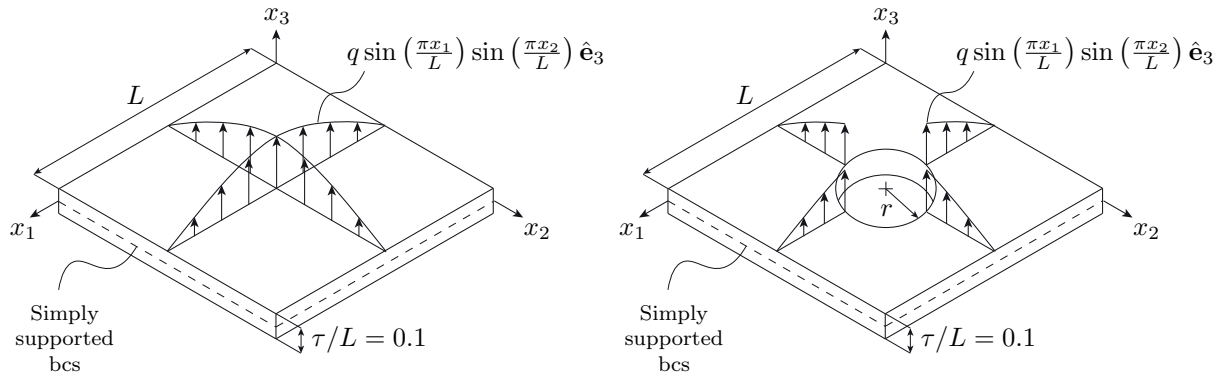

(a) (b)

Figure 3.: Schematic representation of the geometrical features, the applied loads and the enforced boundary conditions of (a) the square plate and (b) the square plate with a central hole employed in the numerical tests.

Furthermore, it can be interesting to investigate how the present dG formulation performs against classical FEM approaches in terms of the overall number of degrees of freedom. Fig.(6) shows the error $e(\boldsymbol{U}_h)$ computed using dG (filled markers) and using quadratic S8R elements implemented in Abaqus [1] (unfilled markers) with default options as a function of the system order. It is possible to note how, clear advantages of the present formulation with respect to FEM are achieved when high-order polynomials are employed.

For the sake of completeness, the higher-order plate theory solutions obtained with the present dG formulation are compared with the exact solutions of 3D elasticity. The comparison is shown in Fig.(7) for the considered plate layups in terms of the displacement components u_1 and u_3 evaluated throughout the thickness of the plate at the coordinates $\{x_1, x_2\} = \{0, L/2\}$ and $\{x_1, x_2\} = \{L/2, L/2\}$, respectively. As expected, in the case of the plates P_1 and P_2, which are homogeneous throughout the thickness, the ED_{444} theory provides a very accurate solution when compared to lower-order theories, whereas, in the case of the multilayered plate, a relatively higher error is observed. This confirms that ESL theories are not adequate for multilayered plates if high accuracy is needed and that the LW approach could then be employed. However, LW theories are outside the scope of this work and will be considered in a future study.

5.2. *Square plate with circular cutout*

The second set of tests are performed on the square plate with the circular cutout shown in Fig.(3b). Also in this case, a cartesian mesh grid is used. However, the mesh is now utilized as a background grid and the presence of the cutout is resolved by means of the implicitly defined mesh technique introduced in Sec.(4). The main steps to construct the implicit mesh for this

specific case are as follows. Fig.(8a) shows the modeling domain Ω and a sample 8×8 background mesh grid. With reference to Eq.(28), the domain Ω is implicitly defined by a suitable distance function ϕ. Here, the following distance function is employed

$$\phi(\boldsymbol{x}) = \pm \min_{\boldsymbol{y}\in\partial\Omega} ||\boldsymbol{x}-\boldsymbol{y}||, \tag{33}$$

where $\boldsymbol{x} = \{x_1, x_2\}$ is the generic point belonging to $\mathbb{R}^2$ and the $+$ or $-$ sign is selected if $\boldsymbol{x}$ is outside or inside Ω. Figure (8b) shows the contour plot of the distance function obtained when Eq.(33) is applied to the considered problem of the plate with a circular cutout; from the colorbar reported in the figure, it is possible to note that the boundaries correspond to the zero of the considered distance function.

As described in Sec.(4), the cells of the background grid are subdivided into empty, partial and entire cells on the basis of their position with respect to the domain Ω, i.e. on the basis of the value of the distance function over the cells themselves. In case of the 8×8 mesh grid, this subdivision is shown in Fig.(8c); then, the final mesh elements are formally defined through Eq.(29) and are drawn in Fig.(8d). It is worth noting that, from the implementation point of view, the partial mesh elements are never explicitly computed nor parametrized and the corresponding stiffness matrices are evaluated using the quadrature technique developed in [44].

Fig.(8e) shows the same subdivision in case of a 10×10 mesh grid; in such a case, some partial cells are deemed small as they fall inside the domain Ω for a very small fraction. To avoid the presence of these small elements, which would increase the condition number of the final stiffness matrix, they are merged with suitably chosen neighboring elements, which are subsequently referred to as extended elements. The final element subdivision in case of a 10×10 mesh grid is drawn in Fig.(8f). Also in this case, extended elements are never explicitly constructed but their contribution to the stiffness matrix is computed by neighboring information only.

Three plate theories are considered, namely the FSDT, the ED_{222} theory and the ED_{444} theory. The solution is computed with the dG formulation by means of the 10×10 mesh grid shown in Fig.(8e) and polynomial order $p = 6$. The results are compared with those obtained with Abaqus by means of quadratic S8R elements for the FSDT and by means of C3D20R elements for the fully 3D analysis.

Figure (9) shows the displacement components u_1 and u_3 evaluated throughout the thickness of the plate at the point $\{x_1, x_2\} = \{L/2 - r, L/2\}$ for the three different plate theories. Figures (9a) and (9b) refer to the isotropic and orthotropic plates, respectively. In both cases, it is

possible to notice that the ED_{444} provides a very accurate solution, with a difference smaller than 0.03%.

Figure (10) shows the contour plots of the displacement component u_3 and of the stress component σ_{22} computed over the top surface of the isotropic plate, i.e. at $x_3 = \tau/2$, considering the FSDT. In the figure, the dashed contour levels refer to the FEM solution obtained, whereas the continuous contour levels refer to the solution computed using the dG approach. The results show a satisfactory accuracy of the present formulation in terms of both the displacement component and the stress component.

Similarly, Fig.(11) shows the contour plots of the displacement component u_3 and of the stress components σ_{11}, σ_{22} and σ_{12} computed over the top surface of the orthotropic plate considering the FSDT. Also in this case, the dashed contour levels refer to the FEM solution, whereas the continuous contour levels refer to the dG solution; a satisfactory accuracy is observed for both the displacement and the stresses.

Lastly, Fig.(12) shows the contour plots of the displacement component u_3 and of the stress components σ_{11}, σ_{22} and σ_{12} computed over the top surface of the orthotropic plate when the dG ED_{444} and the fully FEM 3D solutions are considered. The obtained results show a satisfactory overall accuracy but small discrepancies are observed between the values of σ_{12} computed by the 3D FEM and those computed using the ED_{444} theory in proximity of the points $\{x_1, x_2\} = \{L/2, L/2 \pm r\}$.

6. Conclusion and future developments

In this work, an Interior Penalty discontinuous Galerkin formulation has been developed for higher-order plate theories within the framework of the GUF and the ESL approach.

The formulation has been employed to study the elastic response of a square plate and a square plate with a central circular cutout subjected to an out-of-plane bisinusoidal load. The numerical results on the square plate have been reported to investigate the effect of the penalty parameter and to show that the present technique offers optimal *hp*-convergence and remarkable savings with respect to classic FEM approach when higher-order polynomials are employed.

On the other hand, the numerical results on the plate with the circular cutout have been presented to test the combination of the present dG formulation and the implicitly defined mesh technique proposed by Saye [44, 45, 46]. This approach has the advantage of reducing the meshing effort when complex geometries are considered since the mesh elements are able to resolve with high-order accuracy the boundaries of the domain despite they are never explicitly

constructed. Such a meshing technique would require some further effort in case it were employed within continuous discretization approaches.

However, the developed model still presents some limitations and offers directions of further investigation. First of all, the presented Interior Penalty dG formulation has introduced the penalty parameter μ, see Eq.(24). As shown in the numerical tests, the value of the penalty parameter affects the error of the obtained results and must be typically chosen as a function of the mesh size h. Then it could be interesting to investigate different dG formulations, e.g. the Local or the Compact discontinuous Galerkin methods [2, 40], which, in some cases, only require the positiveness of μ regardless of the mesh size.

As a second remark, the numerical results have shown that, in the case of the orthotropic plate with a central circular hole, the large ratio between the elastic constants of the orthotropic material induced a significant stress concentration around the hole. In this case, the proposed dG formulation could be coupled with selective mesh refinement through hierarchical meshes that would improve the accuracy without excessively increasing the computational cost of the method.

As regards the framework of higher-order plate theories, another direction of further investigation would be the extension of the present dG formulation to Layer Wise models involving either the PVD or the RMVT, which would definitely improve the accuracy of the considered theory throughout the thickness of the plate. On the other hand, numerical tests have been reported with relatively thick plates and, therefore, it would also be interesting to include the thin-plate limit within the present formulation.

Eventually, directions of further studies, which would benefit from the developed implicit mesh discontinuous Galerkin formulation, could include linear eigenvalue and buckling analyses as well as non-linear post-buckling problems of multilayered plate with complex holes or cutouts.

7. Acknowledgements

The authors gratefully acknowledge the support of CINECA's staff for the use of CINECA's HPC facilities

References

[1] *ABAQUS 6.14 Documentation.* Dassault Systèmes, 2014. Providence, RI, USA.

[2] D. N. Arnold, F. Brezzi, B. Cockburn, and L. D. Marini. Unified analysis of discontinuous

galerkin methods for elliptic problems. *SIAM journal on numerical analysis*, 39(5):1749–1779, 2002.

[3] D. N. Arnold, F. Brezzi, and L. D. Marini. A family of discontinuous galerkin finite elements for the reissner–mindlin plate. *Journal of Scientific Computing*, 22(1-3):25–45, 2005.

[4] G. Becker and L. Noels. A full-discontinuous galerkin formulation of nonlinear kirchhoff–love shells: elasto-plastic finite deformations, parallel computation, and fracture applications. *International Journal for Numerical Methods in Engineering*, 93(1):80–117, 2013.

[5] P. R. Bösing, A. L. Madureira, and I. Mozolevski. A new interior penalty discontinuous galerkin method for the reissner–mindlin model. *Mathematical Models and Methods in Applied Sciences*, 20(08):1343–1361, 2010.

[6] E. Carrera. Theories and finite elements for multilayered, anisotropic, composite plates and shells. *Archives of Computational Methods in Engineering*, 9(2):87–140, 2002.

[7] E. Carrera. Theories and finite elements for multilayered plates and shells: a unified compact formulation with numerical assessment and benchmarking. *Archives of Computational Methods in Engineering*, 10(3):215–296, 2003.

[8] E. Carrera and L. Demasi. Classical and advanced multilayered plate elements based upon pvd and rmvt. part 1: Derivation of finite element matrices. *International Journal for Numerical Methods in Engineering*, 55(2):191–231, 2002.

[9] E. Carrera and L. Demasi. Classical and advanced multilayered plate elements based upon pvd and rmvt. part 2: Numerical implementations. *International Journal for Numerical Methods in Engineering*, 55(3):253–291, 2002.

[10] E. Carrera, M. Cinefra, M. Petrolo, and E. Zappino. *Finite element analysis of structures through unified formulation*. John Wiley & Sons, 2014.

[11] M. Cinefra and S. Valvano. A variable kinematic doubly-curved mitc9 shell element for the analysis of laminated composites. *Mechanics of Advanced Materials and Structures*, 23 (11):1312–1325, 2016.

[12] B. Cockburn and C.-W. Shu. The local discontinuous galerkin method for time-dependent convection-diffusion systems. *SIAM Journal on Numerical Analysis*, 35(6):2440–2463, 1998.

[13] G. Davi and A. Milazzo. Boundary element solution for free edge stresses in composite laminates. *Journal of Applied Mechanics, Transactions ASME*, 64(4):877–885, 1997.

[14] G. Davi and A. Milazzo. Bending stress fields in composite laminate beams by a boundary integral formulation. *Computers and Structures*, 71(3):267–276, 1999.

[15] L. Demasi. Treatment of stress variables in advanced multilayered plate elements based

upon reissners mixed variational theorem. *Computers & structures*, 84(19-20):1215–1221, 2006.

[16] L. Demasi. ∞^3 hierarchy plate theories for thick and thin composite plates: the generalized unified formulation. *Composite Structures*, 84(3):256–270, 2008.

[17] L. Demasi. ∞^6 mixed plate theories based on the generalized unified formulation. part i: governing equations. *Composite Structures*, 87(1):1–11, 2009.

[18] L. Demasi. ∞^6 mixed plate theories based on the generalized unified formulation.: Part ii: Layerwise theories. *Composite Structures*, 87(1):12–22, 2009.

[19] L. Demasi. Invariant finite element model for composite structures: The generalized unified formulation. *AIAA journal*, 48(8):1602–1619, 2010.

[20] M. DOttavio. A sublaminate generalized unified formulation for the analysis of composite structures. *Composite Structures*, 142:187–199, 2016.

[21] M. D'Ottavio, L. Dozio, R. Vescovini, and O. Polit. Bending analysis of composite laminated and sandwich structures using sublaminate variable-kinematic ritz models. *Composite Structures*, 155:45–62, 2016.

[22] E. N. Dvorkin and K.-J. Bathe. A continuum mechanics based four-node shell element for general non-linear analysis. *Engineering computations*, 1(1):77–88, 1984.

[23] G. Engel, K. Garikipati, T. Hughes, M. Larson, L. Mazzei, and R. L. Taylor. Continuous/discontinuous finite element approximations of fourth-order elliptic problems in structural and continuum mechanics with applications to thin beams and plates, and strain gradient elasticity. *Computer Methods in Applied Mechanics and Engineering*, 191(34): 3669–3750, 2002.

[24] A. Ferreira. Thick composite beam analysis using a global meshless approximation based on radial basis functions. *Mechanics of Advanced Materials and Structures*, 10(3):271–284, 2003.

[25] A. Ferreira, E. Carrera, M. Cinefra, C. Roque, and O. Polit. Analysis of laminated shells by a sinusoidal shear deformation theory and radial basis functions collocation, accounting for through-the-thickness deformations. *Composites Part B: Engineering*, 42(5):1276–1284, 2011.

[26] A. Ferreira, E. Carrera, M. Cinefra, E. Viola, F. Tornabene, N. Fantuzzi, and A. Zenkour. Analysis of thick isotropic and cross-ply laminated plates by generalized differential quadrature method and a unified formulation. *Composites Part B: Engineering*, 58:544–552, 2014.

[27] S. Güzey, H. Stolarski, B. Cockburn, and K. Tamma. Design and development of a discontinuous galerkin method for shells. *Computer Methods in Applied Mechanics and Engineering*, 195(25-28):3528–3548, 2006.

[28] C. Hwu. Boundary integral equations for general laminated plates with coupled stretching–bending deformation. In *Proceedings of the Royal Society of London A: Mathematical, Physical and Engineering Sciences*, volume 466, pages 1027–1054. The Royal Society, 2010.

[29] R. M. Jones. *Mechanics of composite materials*. CRC press, 1998.

[30] T. Kant and B. Pandya. A simple finite element formulation of a higher-order theory for unsymmetrically laminated composite plates. *Composite Structures*, 9(3):215 – 246, 1988.

[31] V. G. Kirchhoff. Über das gleichgewicht und die bewegung einer elastischen scheibe. *Journal fur die reine und angewandte Mathematik*, 40:51–88, 1850.

[32] K. Liew. Solving the vibration of thick symmetric laminates by reissner/mindlin plate theory and thep-ritz method. *Journal of Sound and Vibration*, 198(3):343–360, 1996.

[33] A. Milazzo and V. Oliveri. Post-buckling analysis of cracked multilayered composite plates by pb-2 rayleigh–ritz method. *Composite Structures*, 132:75–86, 2015.

[34] A. Milazzo and V. Oliveri. Buckling and postbuckling of stiffened composite panels with cracks and delaminations by ritz approach. *AIAA Journal*, 55(3):965–980, 2016.

[35] A. Milazzo, I. Benedetti, and V. Gulizzi. An extended ritz formulation for buckling and post-buckling analysis of cracked multilayered plates. *Composite Structures*, 2018.

[36] R. D. Mindlin. Influence of rotatory inertia and shear on flexural motions of isotropic, elastic plates. *Journal of applied mechanics*, 18:31–38, 1951.

[37] L. Noels and R. Radovitzky. A new discontinuous galerkin method for kirchhoff–love shells. *Computer Methods in Applied Mechanics and Engineering*, 197(33-40):2901–2929, 2008.

[38] A. K. Noor and M. D. Mathers. Finite element analysis of anisotropic plates. *International Journal for Numerical Methods in Engineering*, 11(2):289–307, 1977.

[39] N. J. Pagano. Exact solutions for rectangular bidirectional composites and sandwich plates. *Journal of composite materials*, 4(1):20–34, 1970.

[40] J. Peraire and P.-O. Persson. The compact discontinuous galerkin (cdg) method for elliptic problems. *SIAM Journal on Scientific Computing*, 30(4):1806–1824, 2008.

[41] J. Reddy. Free vibration of antisymmetric, angle-ply laminated plates including transverse shear deformation by the finite element method. *Journal of Sound and Vibration*, 66(4): 565–576, 1979.

[42] J. N. Reddy. *Mechanics of laminated composite plates and shells: theory and analysis*. CRC

press, 2004.

[43] E. Reissner. The effect of transverse shear deformation on the bending of elastic plates. *Journal of applied mechanics*, pages A69–A77, 1945.

[44] R. Saye. High-order quadrature methods for implicitly defined surfaces and volumes in hyperrectangles. *SIAM Journal on Scientific Computing*, 37(2):A993–A1019, 2015.

[45] R. Saye. Implicit mesh discontinuous galerkin methods and interfacial gauge methods for high-order accurate interface dynamics, with applications to surface tension dynamics, rigid body fluid-structure interaction, and free surface flow: Part i. *Journal of Computational Physics*, 344:647–682, 2017.

[46] R. Saye. Implicit mesh discontinuous galerkin methods and interfacial gauge methods for high-order accurate interface dynamics, with applications to surface tension dynamics, rigid body fluid-structure interaction, and free surface flow: Part ii. *Journal of Computational Physics*, 344:683–723, 2017.

[47] B. L. Talamini and R. Radovitzky. A discontinuous galerkin method for nonlinear shear-flexible shells. *Computer Methods in Applied Mechanics and Engineering*, 303:128–162, 2016.

[48] A. Y. Tamijani and R. K. Kapania. Chebyshev-ritz approach to buckling and vibration of curvilinearly stiffened plate. *AIAA journal*, 50(5):1007–1018, 2012.

[49] F. Tornabene, N. Fantuzzi, and M. Bacciocchi. The gdq method for the free vibration analysis of arbitrarily shaped laminated composite shells using a nurbs-based isogeometric approach. *Composite Structures*, 154:190–218, 2016.

[50] G. N. Wells and N. T. Dung. A c0 discontinuous galerkin formulation for kirchhoff plates. *Computer Methods in Applied Mechanics and Engineering*, 196(35-36):3370–3380, 2007.

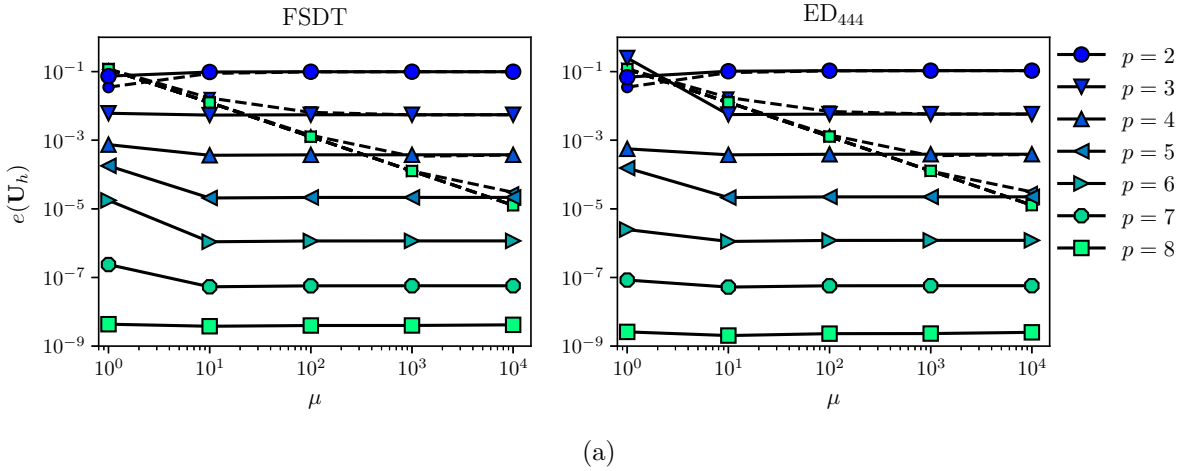

(a)

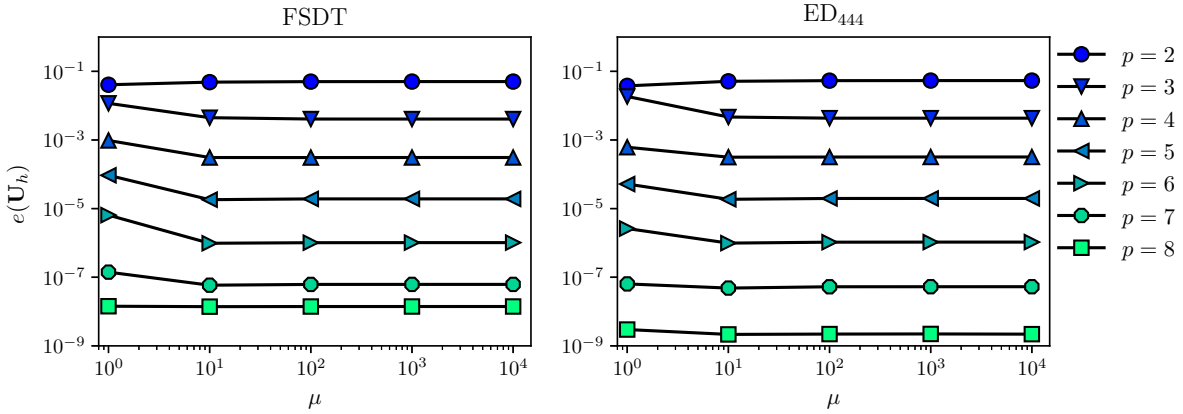

(b)

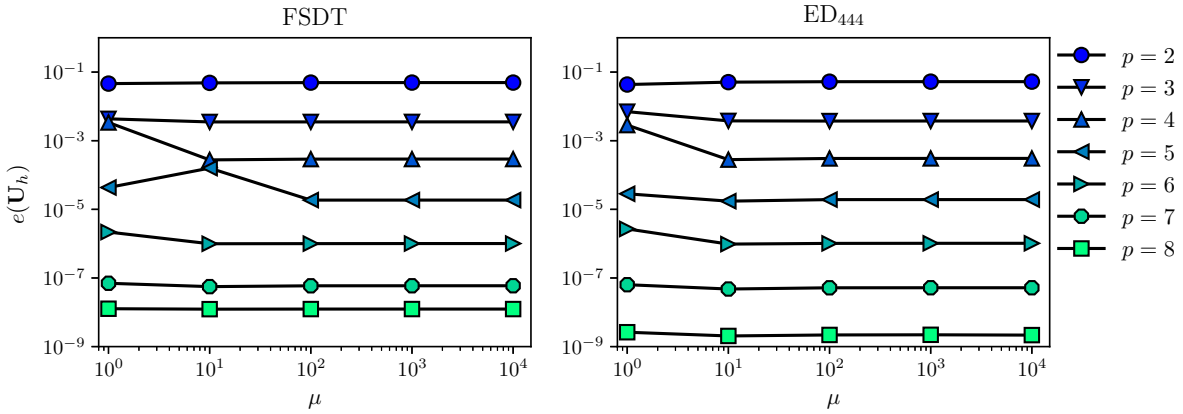

(c)

Figure 4.: Effect of the penalty parameter μ on the ∞-norm error, see Eq.(32), for different plate theories and layups: figures (a), (b) and (c) refer to the P_1, P_2 and P_3 plates, respectively, reported in Table (2). In figure (a), dashed lines with smaller markers are referred to the Penalty method. Data are referred to a 2×2 mesh grid.

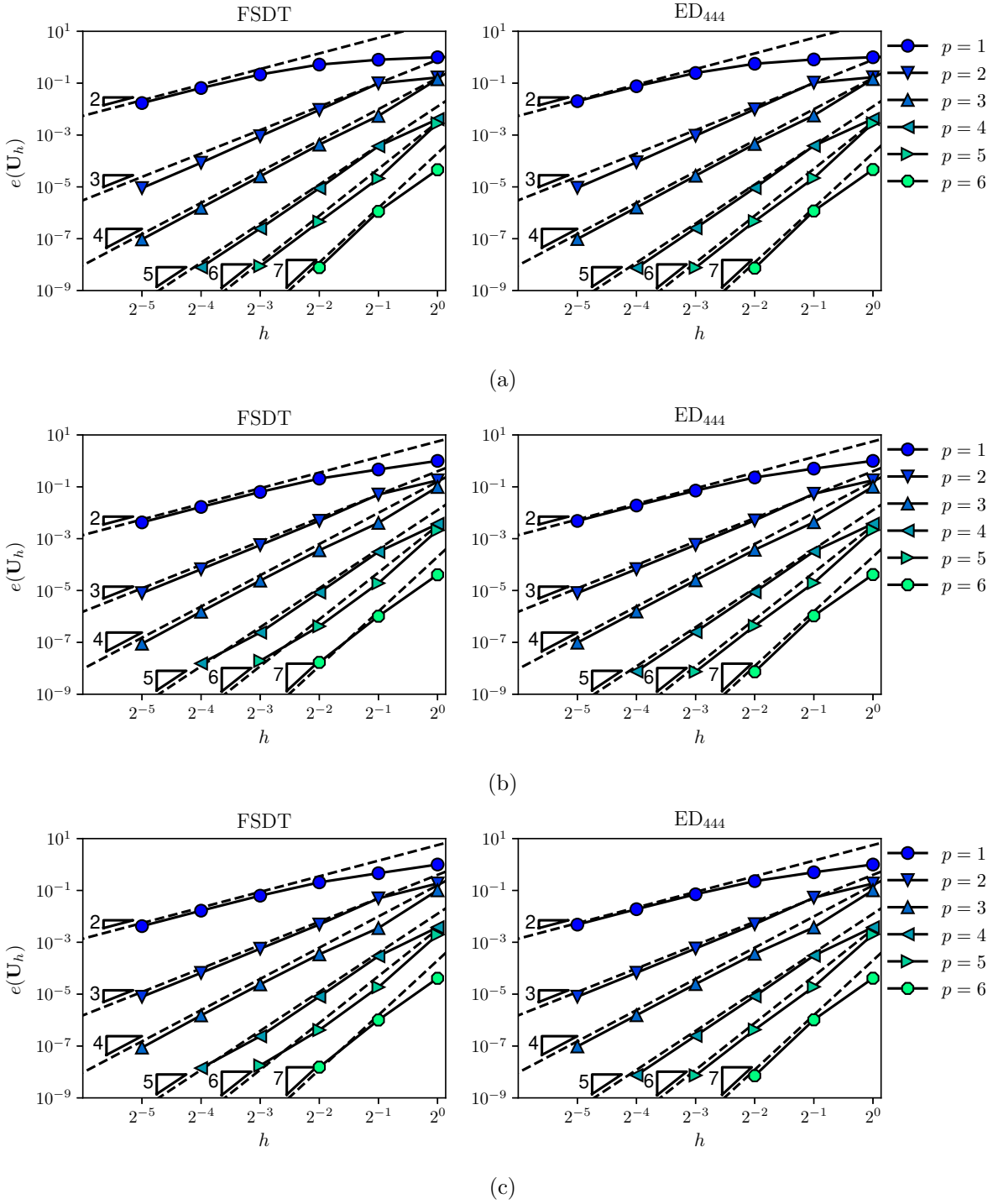

Figure 5.: *hp*-convergence analysis of the ∞-norm error, see Eq.(32), for different plate theories and layups: figures (a), (b) and (c) refer to the P_1, P_2 and P_3 plates, respectively, reported in Table (2). The penalty parameter is set to $\mu = 10/h$ for the plate P_1 and $\mu = 250/h$ for the plates P_2 and P_3.

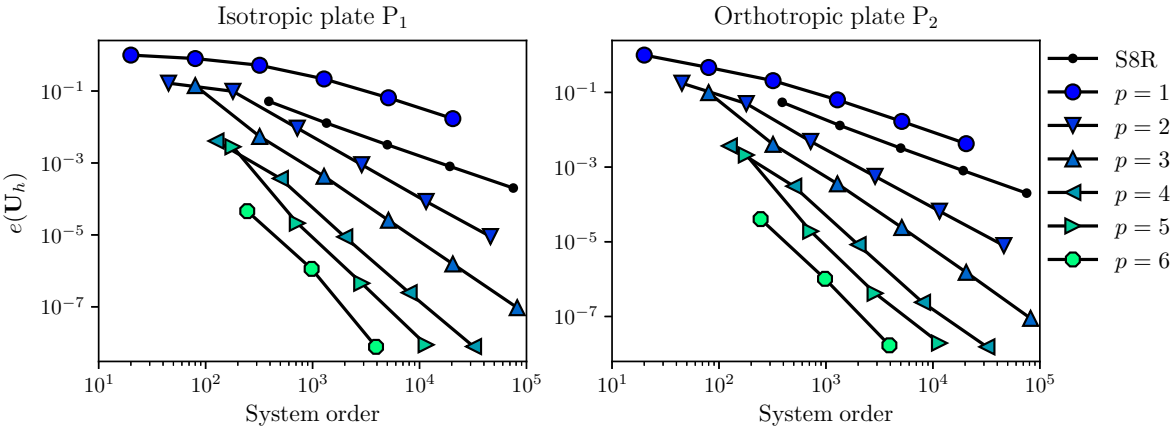

Figure 6.: Comparison between the present dG formulation and standard FEM in terms of the ∞-norm error as a function of the system order.

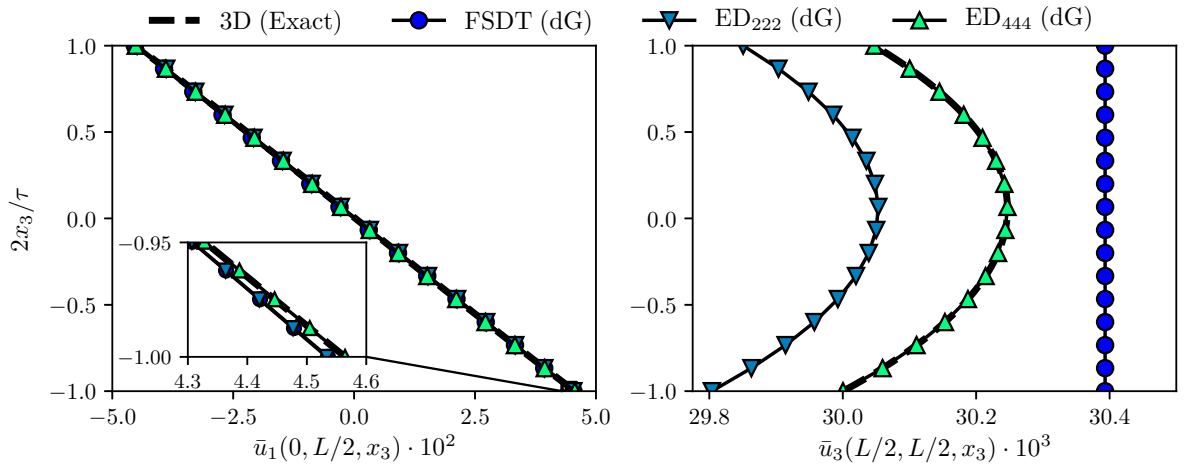

(a)

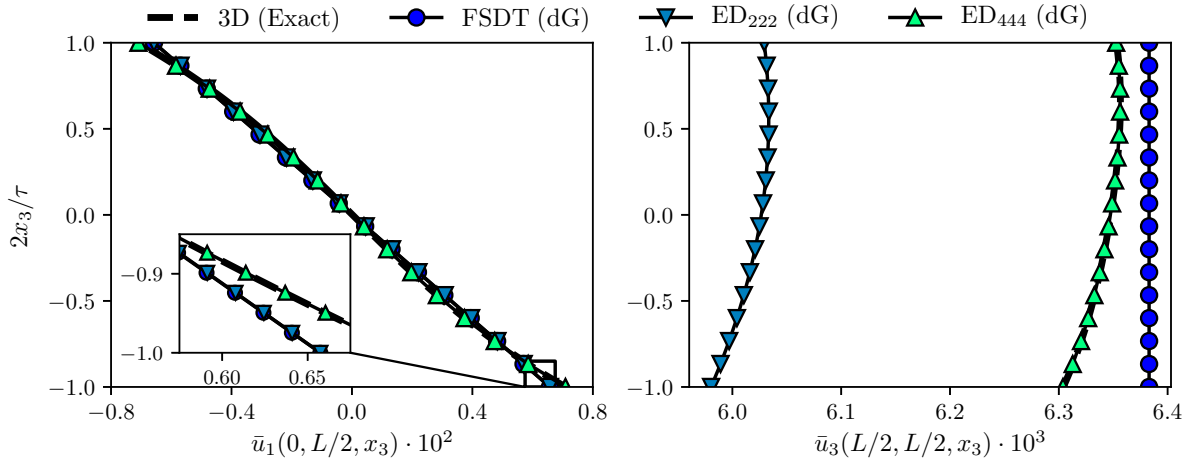

(b)

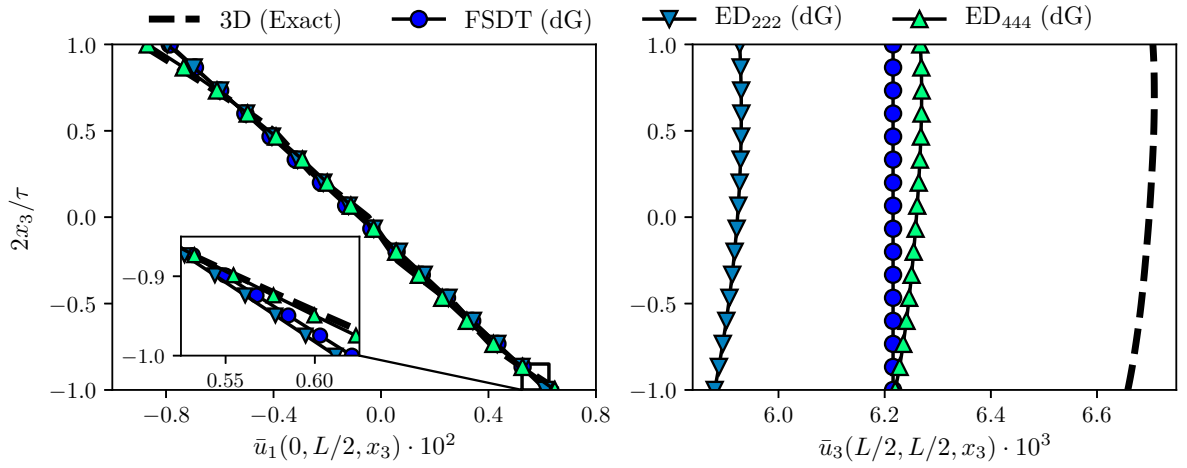

(c)

Figure 7.: Comparison between exact 3D solutions and dG higher-order plate theories solutions in terms of through-the-thickness displacement components u_1 and u_3 evaluated at $\{x_1, x_2\} = \{0, L/2\}$ and $\{x_1, x_2\} = \{L/2, L/2\}$, respectively. Figures (a), (b) and (c) refer to the P_1, P_2 and P_3 plates, respectively, reported in Table (2). The results computed using the present dG method are obtained with a 2×2 mesh grid.

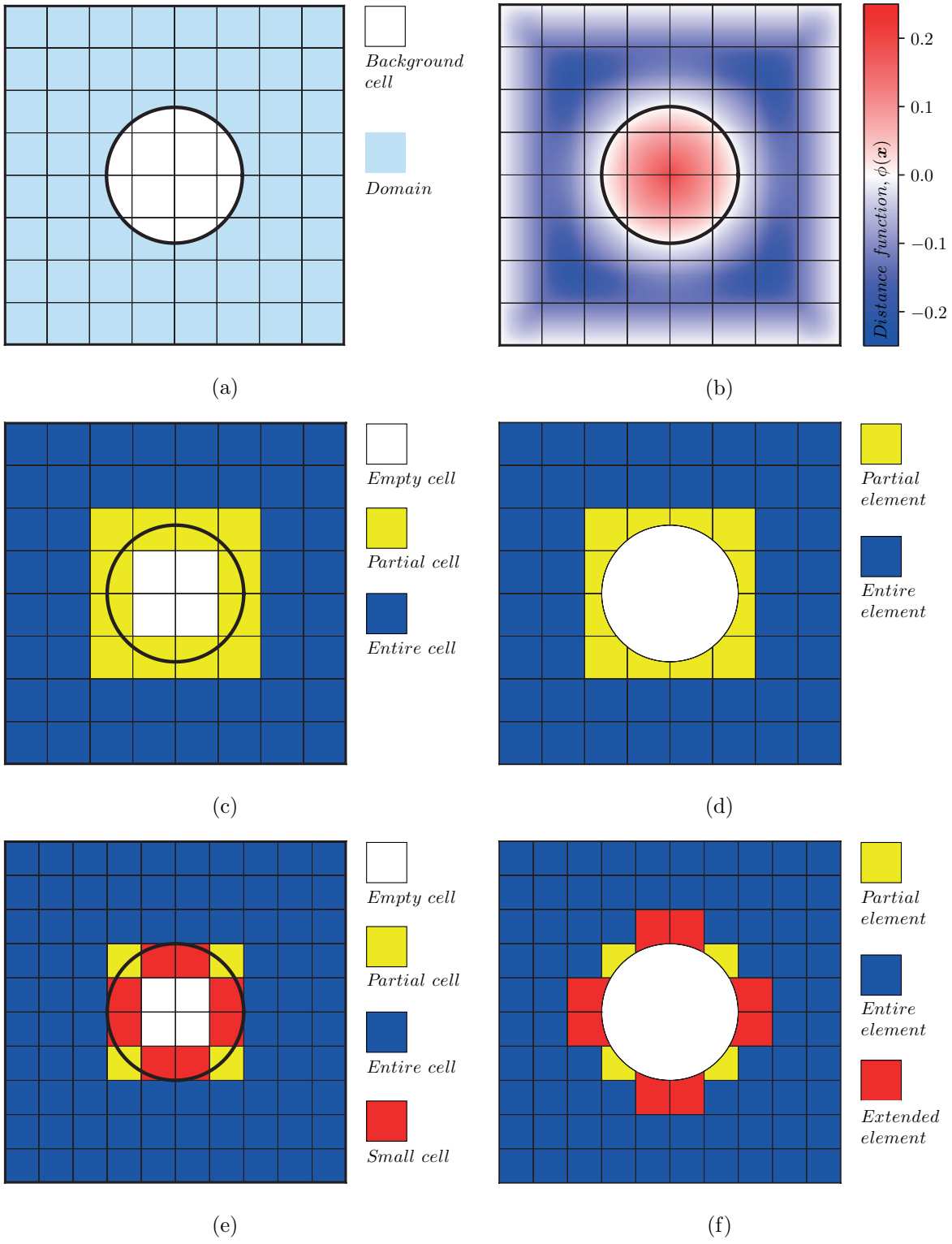

Figure 8.: Implicitly defined mesh construction for a square plate with a central hole: (a) Domain of analysis Ω (in cyan) embedded in a background 8×8 quad grid; (b) Contour plot of the signed distance function $\phi(\boldsymbol{x})$; (c) Background cell classification using a 8×8 quad grid and (d) resulting mesh consisting of entire and partial elements; (e) Background cell classification using a 10×10 quad grid and (f) resulting mesh consisting of entire, partial and extended elements to avoid the presence of overly small elements. It is worth noting that figures (d) and (f) have been generated for illustrative purposes: partial or extended elements are never explicitly constructed during the computation of the stiffness matrices.

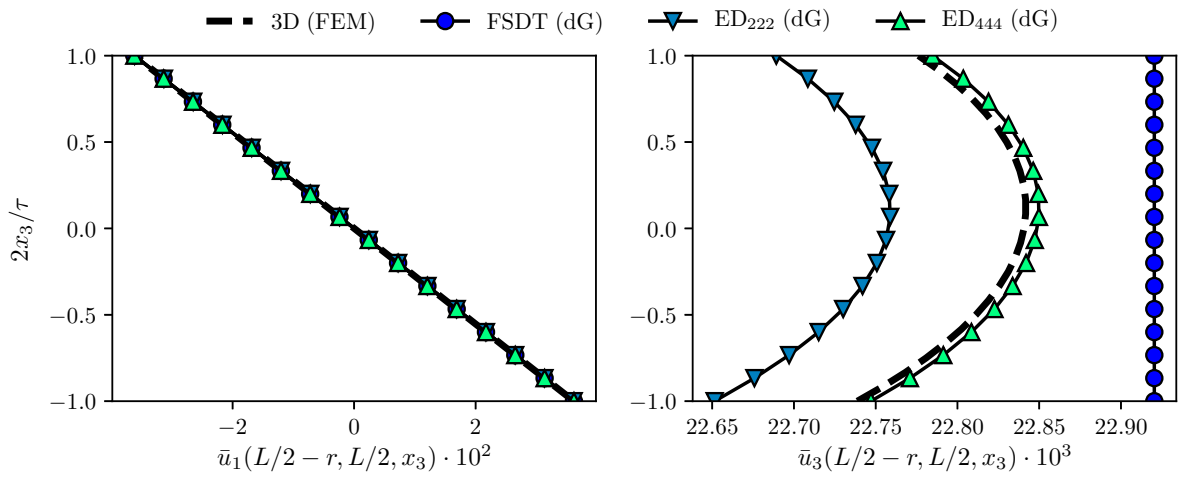

(a)

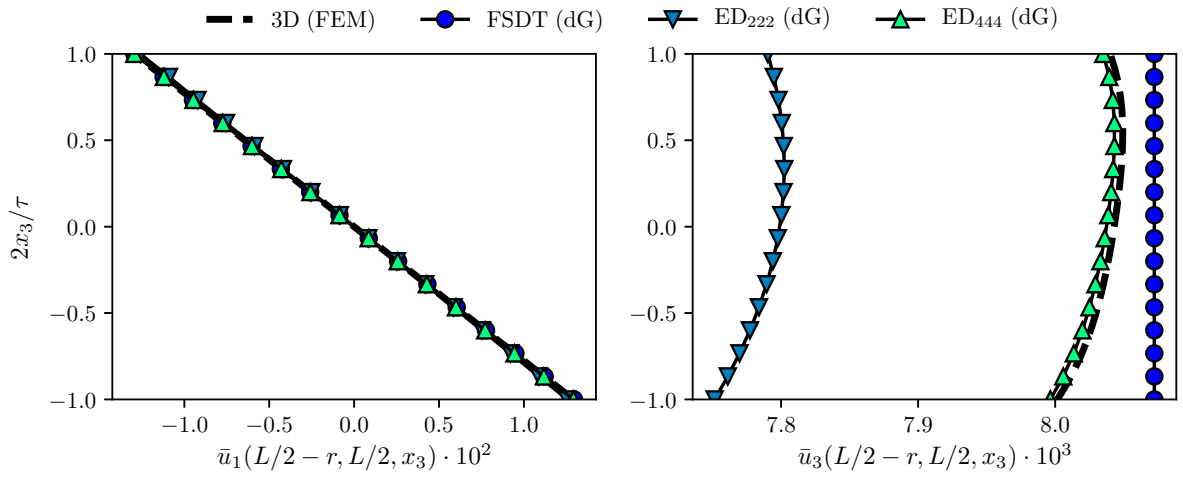

(b)

Figure 9.: Comparison between FEM 3D solutions and dG higher-order plate theories solutions in terms of through-the-thickness displacement components u_1 and u_3 evaluated at $\{x_1, x_2\} = \{L/2-r, L/2\}$. Figures (a) and (b) refer to the P_1 and P_2 plates, respectively, reported in Table (2). The results computed using the present dG method are obtained with the 10×10 mesh grid shown in Fig.(8e).

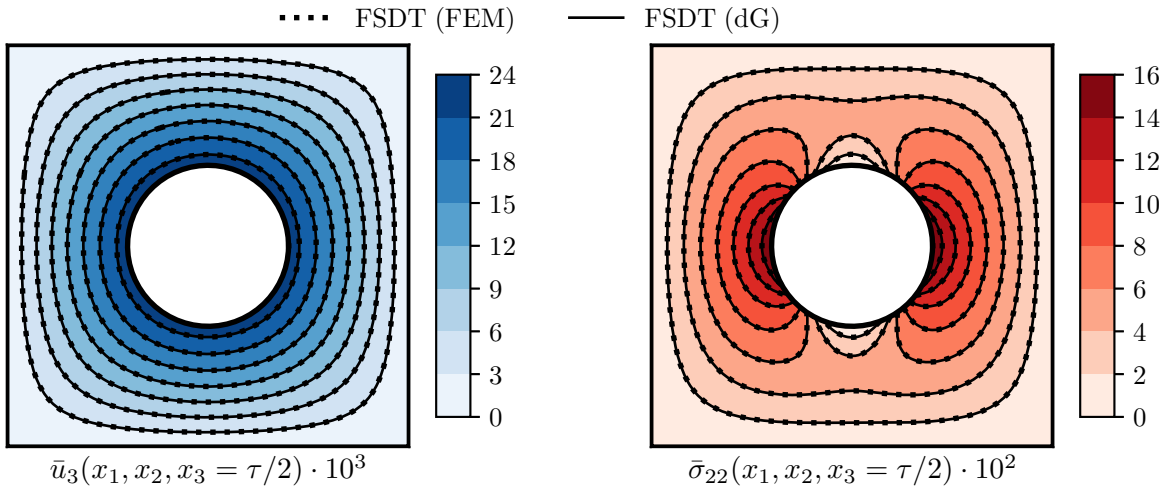

Figure 10.: Comparison between FEM FSDT solution and dG FSDT solution in terms of contour plots of the displacement component u_3 and the stress component σ_{22} over the top surface of the isotropic single-layer plate, whose properties are reported in Table (2). The results computed using the present dG method are obtained with the 10×10 mesh grid shown in Fig.(8e).

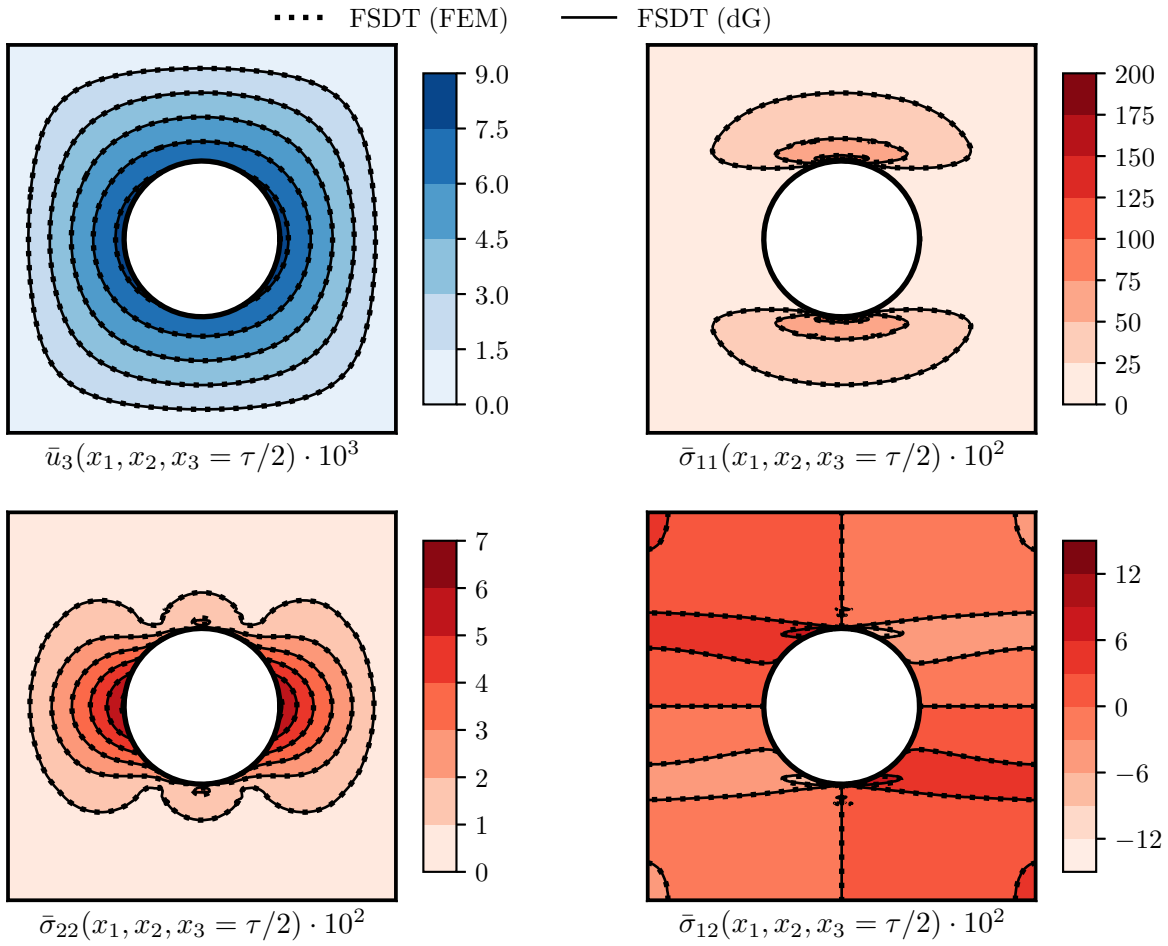

Figure 11.: Comparison between FEM FSDT solution and dG FSDT solution in terms of contour plots of the displacement component u_3 and the stress components σ_{11}, σ_{22} and σ_{12} over the top surface of the orthotropic single-layer plate, whose properties are reported in Table (2). The results computed using the present dG method are obtained with the 10×10 mesh grid shown in Fig.(8e).

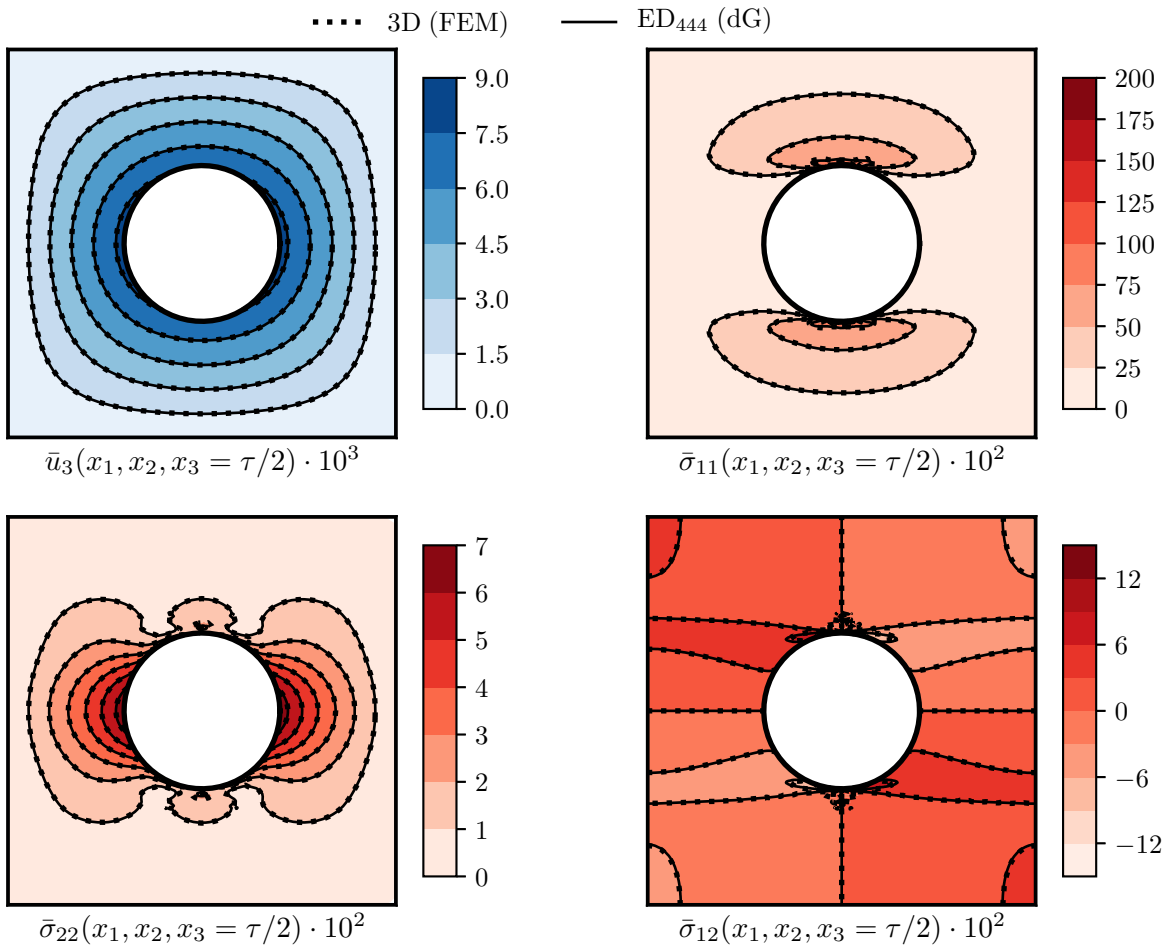

Figure 12.: Comparison between FEM 3D solution and dG ED_{444} solution in terms of contour plots of the displacement component u_3 and the stress components σ_{11}, σ_{22} and σ_{12} over the top surface of the orthotropic single-layer plate, whose properties are reported in Table (2). The results computed using the present dG method are obtained with the 10×10 mesh grid shown in Fig.(8e).

View publication stats